Strength of TROPOMI satellite observations in retrieving hourly resolved sources of volcanic sulfur dioxide by inverse modeling

Abhinna K. Behera[1], Marie Boichu[1], François Thieuleux[1], Nicolas Henriot[1], and Souichiro Hioki[1]

[1]Univ. Lille, CNRS, UMR 8518 - LOA - Laboratoire d'Optique Atmosphérique, F-59000 Lille, France

Correspondence: Abhinna K. Behera (abhinna.behera@univ-lille.fr)

Abstract. Volcanic eruptions release sulfur dioxide (SO_2), impacting air quality, ecosystems, and aviation. To comprehensively assess these effects, high-temporal-resolution SO_2 emission data is crucial. In this study, we use an inverse modeling procedure, assimilating SO_2 column measurements from TROPOMI and OMPS low-Earth orbit satellites into an Eulerian chemistry-transport model. This procedure allows us to derive precise hourly SO_2 mass flux and injection heights. TROPOMI,
5   with its exceptional spatial resolution, excels at detecting short-lived, concentrated SO_2 plumes near the source shortly before satellite overpasses. This high-resolution data enables more robust identification and precise characterization of strong SO_2 emissions, surpassing the capabilities of lower-resolution OMPS measurements, which may overlook or underestimate vigorous degassing periods. Notably, this high-resolution data also facilitates the detection of pre-eruptive SO_2 emissions. Cloud cover can obscure SO_2 plumes from satellite observations, but our inverse modeling procedure effectively distinguishes
10   and tracks them by assimilating successive satellite overpass data. Furthermore, this procedure proves less susceptible to ash emissions compared to geostationary Himawari-8/AHI observations. We apply our methodology to study the 2018 Ambrym eruption, a former major volcanic SO_2 emitter. This eruption marked the end of long-lived lava lake activity and initiated a submarine eruption through a massive magma intrusion. Our detailed SO_2 flux time series unveils the evolution of the eruption and identifies distinct SO2 sources, including lava flows and shallow magma intrusions. In summary, the assimilation
15   of TROPOMI data into inverse modeling procedures offers significant potential for enhancing our understanding of magma transport and environmental impacts during volcanic eruptions.

1 Introduction

Volcanic sulfur dioxide (SO_2) emissions offer insights into subterranean magma and volatile dynamics, as well as interactions
20   with hydrothermal systems (Oppenheimer et al., 2011, 2014; Edmonds et al., 2003). Additionally, these emissions have multifaceted atmospheric impacts, including air quality degradation (Hansell and Oppenheimer, 2004; Boichu et al., 2016, 2019), ecological effects (Delmelle et al., 2002), and health concerns for both humans and animals (Stewart et al., 2021). They can lead to respiratory issues, exacerbate pre-existing conditions, and harm vegetation (Cronin and Sharp, 2002; Allibone et al., 2012;

Mueller et al., 2020; Thorsteinsson et al., 2012). Large quantities of sulfate aerosols resulting from SO_2 oxidation, whether
25 through direct or indirect mechanisms, can influence the climate (Robock, 2000; Kremser et al., 2016; Marshall et al., 2022).
Moreover, volcanic emissions pose a hazard to aviation, impacting aircraft visibility (Guffanti et al., 2010a; Weinzierl et al.,
2012) and causing damage to aircraft engines due to corrosive sulfate deposition (Prata and Tupper, 2009; Prata, 2009; Carn
et al., 2009; Guffanti et al., 2010b).

Monitoring volcanoes, especially SO_2 emissions, is therefore essential for accurate hazard assessment. To achieve this, we
30 must precisely estimate key emission parameters, including SO_2 mass flux and injection height, with high temporal resolution
(e.g., Thomas and Watson, 2010; Boichu et al., 2015). As SO_2 is an unambiguous indicator of volcanic plume, these parameters
become vital inputs for chemistry-transport models (CTM), enabling accurate simulations of volcanic SO_2, ash, and sulfate
aerosol dispersion to assess atmospheric hazards. Additionally, detailed emission data provides valuable insights into magma
dynamics and can potentially reveal precursor signals of impending eruptions (e.g., Sparks, 2003; Oppenheimer, 2010; Kilbride
35 et al., 2016).

Remote sensing methods excel in detecting volcanic SO_2 due to its unique spectral signature and relatively low background
atmospheric concentration. Since 1978, low-Earth polar-orbiting (LEO) ultraviolet (UV) and infrared (IR) hyperspectral sen-
sors have continuously observed global bulk SO_2 levels (Carn et al., 2017), albeit with limited temporal coverage, providing
daily or bi-daily SO_2 column images. Complementing LEO observations, geostationary sensors offer more frequent measure-
40 ments despite lower spectral resolution and sensitivity to SO_2 gas concentration (Prata and Grant, 2001; Prata et al., 2007;
Corradini et al., 2021). Furthermore, ground-based UV DOAS spectrometers have monitored volcanic plumes effectively since
the early 2000s, particularly adept at detecting low-altitude and weak to moderate SO_2 degassing, crucial for pre-eruptive mon-
itoring (Campion et al., 2012; Arellano et al., 2021). Nevertheless, ground-based volcano monitoring poses significant chal-
lenges, encompassing financial constraints, logistical difficulties, installation, equipment upkeep, and local personnel training.
45 The Network for Observation of Volcanic and Atmospheric Change (NOVAC) has coordinated efforts to monitor volcanoes,
but only 37 out of thousands of active volcanoes possess the necessary instruments (Arellano et al., 2021). These instruments
can also malfunction during eruptions or fail to detect degassing amidst heavy ash emissions (e.g., Surono et al., 2012; Boichu
et al., 2015).

Various methods have emerged for sub-daily tracking of volcanic SO_2 emissions from space. The rough Delta-M approach
50 assesses mass flux by calculating the difference in mass burdens between consecutive acquisitions and dividing by the time in-
terval (Theys et al., 2013). A more refined technique, known as the traverse method, estimates SO_2 mass flux by multiplying the
plume's SO_2 amount cross-section by its velocity, derived from external sources and assumed to match the plume altitude wind
speed (Carn and Bluth, 2003; Merucci et al., 2011; Theys et al., 2013). Another set of methods, employed to determine monthly
mean SO_2 lifetime and emission rate, involves fitting an exponentially modified Gaussian function to the monthly mean column
55 amount as a function of distance from the source, as documented by Beirle et al. (2014); Fioletov et al. (2016, 2017, 2020);
Carn et al. (2017). It is important to note that all these techniques rely on assumptions about plume dispersion and wind fields,
rendering them unsuitable for cases involving intricate wind patterns.

Using atmospheric (Lagrangian) trajectory models in a backward mode provides an alternative approach for estimating volcanic SO_2 emission parameters from LEO satellite observations at high temporal resolution. This method initially determines the height of plume parcels and then calculates the time- and height-resolved mass of emissions for each parcel. Notably, this approach, as demonstrated by previous studies (e.g., Hughes et al., 2012; Pardini et al., 2017; Queißer et al., 2019; Cai et al., 2022; Esse et al., 2023), faces challenges related to plume recirculation. For example, Queißer et al. (2019) compare TROPOMI SO_2 column images to ground-based measurements and back-trajectory calculations, and report that they agree well, fairly well, and satisfactorily for monthly, daily, and intra-diurnal averages, respectively. Additionally, assimilating individual LEO satellite images using these methods does not allow for resolving potential trade-offs between injection height and time without a priori assumptions on the eruption timing.

The inverse modeling procedure, while computationally demanding, efficiently addresses these challenges by assimilating multiple successive satellite images of the dispersed SO_2 plume in a single operation (e.g., Boichu et al., 2013, 2015; Theys et al., 2013; Stohl et al., 2011; Eckhardt et al., 2008). This method involves identifying the volcanic ash and/or SO_2 source term that minimizes differences between observed and simulated gas/particle column amounts at each satellite pixel (e.g., Eckhardt et al., 2008; Kristiansen et al., 2010; Stohl et al., 2011; Theys et al., 2013; Boichu et al., 2013, 2014, 2015; Moxnes et al., 2014; Zidikheri and Potts, 2015; Heng et al., 2016). Simulations use either transport or chemistry-transport models to describe atmospheric physico-chemical processes affecting released SO_2 parcels from the volcanic source until satellite acquisition. The hourly retrieval of height-resolved SO_2 mass flux emissions through an inverse modeling procedure, which does not require a priori assumptions of emissions profiles, has been validated against ground-based UV DOAS observations, demonstrating resilience to strong ash emissions (Boichu et al., 2015). In the same vein, 4D-Var data assimilation procedures have been developed (Flemming and Inness, 2013; Vira et al., 2017).

In this study, we illustrate the enhanced accuracy of SO_2 source retrieval using an inverse modeling procedure by assimilating high-spatial-resolution SO_2 observations from the Sentinel-5P/TROPOMI satellite (Theys et al., 2017, 2019), in contrast to coarser SO_2 observations from Suomi-NPP/OMPS (Flynn et al., 2006, 2014) (sect. 2). It is important to clarify that the term "assimilation" in this context refers to a simplified representation of the linear least-squares optimization applied in a retrospective analysis procedure. We improve emissions parameters accuracy and compare results with high-temporal-resolution geostationary measurements from Himawari-8/AHI, which offer qualitative SO_2 flux estimates (sect. 3). Our work demonstrates that sequential data assimilation effectively simulates the presence of SO_2-rich plumes beneath meteorological clouds (sect. 3), opening new avenues for enhancing volcanic plume forecast reliability. As a case study, we examine the 2018 eruption of the Ambrym volcano, which had been a significant continuous SO_2 emitter for the recent decade, ranking it as the world's top SO_2 emitter until 2018 (Carn et al., 2017; Fioletov et al., 2016, 2023). This volcanic eruption disrupted both the decade-long SO_2 degassing and the persistent lava lake activities associated with this basaltic volcano (Hamling et al., 2019; Shreve et al., 2019). Through our analysis of high-resolution SO_2 degassing data, we gain insights into the intricate magma dynamics that occurred during the 2018 eruption (sect. 4). We show how different magma sources contribute to the degassing observed at the surface, a complexity that can result in contrasted volcanic hazards.

2 Data and research methods

2.1 SO$_2$ columns from low-Earth polar-orbiting UV satellite sensors: TROPOMI and OMPS

LEO satellite sensors provide vertical column density (SO$_2$ column hereafter) images, which represent the number of SO$_2$

95 molecules in an air column per unit area. These images are measured in Dobson Unit (DU), where $1\,\text{DU}$ equals 2.69×10^{16}

molecules/cm^2. In 2018, the TROPOMI science team started to provide a daily SO$_2$ column with a nadir footprint of $7\,\text{km} \times$

$3.5\,\text{km}$ (Veefkind et al., 2012; Theys et al., 2019). Then from August 2019 onwards, it is available with a nadir footprint

of $5.5\,\text{km} \times 3.5\,\text{km}$. This data is obtained using the differential optical absorption spectroscopy (DOAS) algorithm. DOAS

algorithm estimates the SO$_2$ slant column density (SCD) from a measured UV spectrum and subsequently derives the SO$_2$

100 column from the SCD (Theys et al., 2015, 2017). To perform this estimation, the algorithm uses the following ancillary inputs:

air mass factors, scattering weight functions computed by the radiative transfer model assuming a U.S. standard atmosphere,

Lambertian reflecting surface for handling meteorological clouds (Eskes and Boersma, 2003), and a priori SO$_2$ profile given

by the global CTM TM5 (Tracer Model 5, 34 sigma-pressure levels up to $0.1\,\text{hPa}$, Huijnen et al. (2010)). Nevertheless, the

operational DOAS algorithm, sensitive to aerosols and clouds, can lead to spectral misfits, introducing systematic errors in

105 SO$_2$ column retrievals. Recently, Theys et al. (2021) introduced COBRA, a spectral fitting technique similar to the principal

component analysis (PCA) technique used in OMI and OMPS retrievals (Yang et al., 2007, 2013; Li et al., 2017, 2020b),

which reduces biases for weak SO$_2$ columns and eliminates the need for post-processing background correction. COBRA

uses a measurement error covariance matrix to fully represent SO$_2$-free radiance variability, focusing solely on retrieving SO$_2$

SCD. Their study demonstrates that COBRA significantly enhances SO$_2$ column retrievals compared to the current TROPOMI

110 DOAS operational product. Over a 2.5-year analysis with high-resolution TROPOMI data, this approach unveils numerous new

global SO$_2$ emission sources, highlighting COBRA's superior SO$_2$ detection capabilities. However, the SO$_2$ data processed by

this algorithm is currently available only from 2022 onwards. The OMPS sensor, on the other hand, captures SO$_2$ columns at

a coarser spatial resolution, with a nadir footprint size of $50\,\text{km} \times 50\,\text{km}$ (Flynn et al., 2014; Carn et al., 2015). Unlike the

TROPOMI SO$_2$ retrieval method, the estimation of the SO$_2$ column from OMPS uses the PCA technique. The a priori SO$_2$

115 profile used in this process is derived from the Goddard Earth Observing System global 3D model for atmospheric chemistry

(72 sigma-pressure levels up to $0.01\,\text{hPa}$, Bey et al. (2001)). In Theys et al. (2015), the technical details and a comparison

of the DOAS and PCA-based SO$_2$ retrieval methods are presented. They demonstrate a linear relationship between the SO$_2$

columns derived from DOAS and PCA, based on backscattered UV data obtained from the OMI sensor.

For the 2018 Ambrym case study associated with mid-tropospheric SO$_2$ degassing, we assimilate the level 2 SO$_2$ col-

120 umn datasets from TROPOMI and OMPS, namely the $7\,\text{km}$ SO$_2$ product (S5P_OFFL_L2_SO2; Copernicus Sentinel data

processed by ESA (2020)) and the TRM SO$_2$ product (NMSO2_PCA_L2_v2.0; Li et al. (2020a); Zhang et al. (2017)), respec-

tively. We post-process TROPOMI data before assimilation to remove abnormally high SO$_2$ column values ($>1\,\text{DU}$) at the

swath edges. These high values are detected even when there are no nearby SO$_2$ plumes (Fig. S1). We consider the swath edge

as extending 25 ground pixels on either side of the swath. To prevent inaccurate retrievals from interfering with the inverse

125 modeling procedure, we set a specific threshold for the SO$_2$ column values of pixels at the swath edge. This ensures that only

pixels at the swath edge of volcanic origin are considered during the assimilation. We typically adjust the SO_2 threshold for these pixels to be between $1.1\,DU$ to $1.4\,DU$, depending on the day between December 13 and 18 (Fig. S2). Pixels below this threshold are set to zero SO_2 columns. We do not post-process the OMPS SO_2 data.

2.2 Himawari-8/AHI geostationary satellite data

130 Shreve et al. (2019) use the geostationary Himawari-8 satellite's advanced Himawari imager (AHI) to assess the thermal characteristics of the lava flow during the 2018 Ambrym eruption. AHI captures data in six spectral bands spanning the visible and infrared spectrum. The spatial resolution varies, with the visible and near-infrared bands offering approximately $0.5\,km$ to $1\,km$ resolution across Asia and Oceania, while the infrared bands provide a $2\,km$ spatial resolution (Bessho et al., 2016). The calculation of thermal characteristics of lava flow involves combining brightness temperatures (BT) from the $3.9\,\mu m$ and

135 $10.4\,\mu m$ channels (Shreve et al., 2019). Then, to estimate the SO_2 flux proxy, Shreve et al. (2019) integrate pixels showing an SO_2 column proxy exceeding $4°\,K$ within a $50\,km \times 35\,km$ region centered at Ambrym. The calculation of the SO_2 column proxy relies on data from the $10.4\,\mu m$ and $8.5\,\mu m$ channels, collected at 20-minute intervals.

In addition, SO_2/Ash RGB composites can be derived from these channels to infer qualitative knowledge about the SO_2 emissions, as documented in Ishii et al. (2018). These RGB composites (red: $BT_{12.4\mu m}$ - $BT_{10.4\mu m}$, green: $BT_{10.4\mu m}$ - $BT_{8.6\mu m}$,

140 blue: $BT_{10.4\mu m}$) are accessible at the AERIS/ICARE data center (Boichu and Mathurin, 2022). They serve to distinguish SO_2 plumes and volcanic ash. It is important to note that SO_2 RGB images can be affected by clouds, aerosols, and other atmospheric species, leading to false positives or negatives and limiting SO_2 signal isolation (e.g., Prata, 1989; Simpson et al., 2000).

2.3 CHIMERE chemistry-transport model simulation

We use the offline Eulerian CTM CHIMERE (Mailler et al., 2017) to simulate the dispersion of the SO_2-rich plume from the

145 Ambrym eruption during 13–18 December 2018. The meteorological fields for CHIMERE are driven hourly by the Advanced Research WRF model (Powers et al., 2017), an external meteorological model that is constrained by the 0.25-degree ERA-5 reanalysis data (Hersbach et al., 2020) at 37 pressure levels to obtain initial and hourly boundary conditions. A two-week spin-up period is computed to accurately simulate with WRF the complex wind fields in the Indonesian-Australian basin because of the Madden-Julian oscillation (e.g., Feng et al., 2020). Additionally, the top layer of the WRF run is set to $50\,hPa$ to correctly

150 simulate deep convection. The horizontal grid for both the CHIMERE and WRF runs is $10\,km \times 10\,km$, and the vertical extent of the CHIMERE CTM grid reaches $200\,hPa$, which is approximately $12.5\,km$ above sea level (ASL).

We simulate SO_2 concentration by injecting each hour passive tracers at multiple altitudes ranging from $2\,km$ to $11\,km$ ASL, as shown in Fig. S3. The tracers are released following a Gaussian profile at each model level, both in time and in altitude. Ambrym's vent is $1.3\,km$ ASL, so we limit our analysis to emissions above $2\,km$ ASL to capture the eruption's gas emissions.

155 Therefore, we do not expect the CTM simulations to generate an SO_2 plume to the northwest of the source, as driven by the low-level southeasterly trade winds. Additionally, UV sensors are less sensitive to SO_2 below $2\,km$ ASL (e.g., Yang et al., 2010; Theys et al., 2017). The CHIMERE run does not account for SO_2 conversion to sulfate aerosol, nevertheless, the passive

tracers followed all the relevant physical processes in the atmosphere, including transport, diffusion, turbulent mixing, dry deposition, and wet scavenging.

2.4 Assimilating LEO satellite data to estimate SO₂ emissions

2.4.1 Inverting emission profiles

The CHIMERE CTM provides the forward model Jacobian $\mathbf{G}$ (Eq. 1). The $\mathbf{G}$ matrix ($n \times p$) represents the sensitivity of the observation vector $\boldsymbol{d}$ ($n \times 1$) to the state vector $\boldsymbol{m}$ ($p \times 1$), i.e., $G_{ij} = \frac{\partial d_i}{\partial m_j}$. This matrix is determined by simulating tracer transport with the CTM, which incorporates various physical processes and links emissions from the source to LEO satellite-observed SO₂ column data. The satellite observations are compiled in the observation vector $\boldsymbol{d}$, which consists of SO₂ columns from several consecutive satellite overpasses during the Ambrym eruption. Each element of the $\boldsymbol{d}$ vector is associated with a time and spatial coordinate. Inversion of satellite SO₂ columns relies on a large state vector $\boldsymbol{m}$ to constrain the emission with hourly temporal resolution. However, the size of the state vector is constrained by the resolution of the CTM simulation, which in turn depends on its ability to resolve wind fields. Additionally, it is influenced by factors from the observation perspective, such as the measurement footprint size and accuracy. In our case, the state vector $\boldsymbol{m}$ comprises 1200 elements. It represents tracers emitted each hour at specific altitudes, portraying the SO₂ emission of the Ambrym eruption in relation to time and injection height.

We adopt the inverse modeling procedure developed by Boichu et al. (2013, 2014, 2015), which uses linear least-squares optimization without using a priori knowledge of SO₂ emissions to minimize the analysis residuals, i.e., the difference between the forward simulation and the observation. This data assimilation procedure is strongly data-driven, relying solely on the data to determine the optimal estimate ($\hat{m}$). It maximizes the extent to which the data can support the findings as no a priori notions about the SO₂ emissions are used. The optimal estimate $\hat{m}$ is a state vector that minimizes $\|d_i - G_{ij}m_j\|^2$, where d_i and m_j are non-negative and $m_j \in \mathbb{R}^p$ and $d_i \in \mathbb{R}^n$. To account for measurement noise and error in the forward model, we apply the second-order Tikhonov side constraint (Hansen, 1998), which constrains the second derivative of $\boldsymbol{m}$. The equation we solve is

$$\begin{pmatrix} d \\ 0 \end{pmatrix} = \begin{pmatrix} G \\ 10^\lambda \nabla^2 \end{pmatrix} m. \tag{1}$$

The Laplace operator (∇^2) is a tridiagonal matrix representing the discrete second derivative with respect to time. It has a primary diagonal of -2, and the diagonal components above and below have a value of 1. No smoothing is applied with respect to injection heights. The smoothing factor in the inversion is 10^λ. The optimal solution is determined using the L-curve method (Hansen and O'Leary, 1993) (Fig. S4). The emissions ($\hat{m}$) are optimized so that the CTM simulation would fit the observations $\boldsymbol{d}$ while adhering to the restrictions of a non-negative solution (Lawson and Hanson, 1995). Additionally, if the largest element in any row of the $\mathbf{G}$ matrix, $\frac{\partial d_i}{\partial m_j}$, is less than 1×10^{-8}, the entire row and the associated observation in the $\boldsymbol{d}$ vector are removed to maintain the inversion's numerical stability.

To keep the condition number of the $\mathbf{G}$ matrix low and ensure that the inverse problem is numerically stable (Demmel, 1987; Hansen, 1998), we include all zero data points in the observation vector $\boldsymbol{d}$ and the corresponding sensitivity elements in the $\mathbf{G}$ matrix. This implies that we treat zero SO_2 column measurements as valid data to constrain the state vector $\boldsymbol{m}$. Zero SO_2 column pixels can signify either the absence of a volcanic plume or, in certain cases, an undetected SO_2 plume. For instance, pixels falling below the satellite sensor's detection threshold or obscured by clouds may register as zero data points. Consequently, it is essential not to automatically interpret zero data points as evidence of the absence of a volcanic SO_2 plume. Neglecting them during source estimation could lead to inaccuracies.

2.4.2 Post-processing of inverted SO_2 emissions

We use a sifting threshold to eliminate weak SO_2 emissions with a large uncertainty from the optimal emission profile ($\hat{m}$). The threshold is determined by the mean (μ) and standard deviation (σ) of the SO_2 emissions' (m_i) distribution. To retrieve SO_2 emissions from TROPOMI data assimilation, we use the same threshold as for OMPS data assimilation ($\mu + \sigma$). However, further analysis shows that a higher threshold ($\mu + 2\sigma$) could have been used for OMPS data assimilation (see Fig. S5). This distinction arises from OMPS's lower sensitivity to SO_2 compared to TROPOMI, necessitating a higher threshold to filter out poorly constrained weak emissions. We discuss these uncertainties in sect. 4.2.

3 Results

3.1 Hourly SO_2 emissions obtained by inverse modeling: superiority of TROPOMI compared to OMPS

3.1.1 Broad agreement between SO_2 mass-flux time series obtained by assimilating TROPOMI and OMPS column data

The SO_2 mass-flux time series, obtained by assimilating TROPOMI and OMPS SO_2 column data, broadly agree, depicting Ambrym's three-stage eruption between December 13 and 18, 2018 (as shown by the red line for TROPOMI and the blue line for OMPS, see Fig. 1a and 2a). We indicate the three stages of the eruption as follows: first stage – 12:00 UT December 14 to 18:00 UT December 15; second stage – 18:00 UT December 15 to 13:00 UT December 16; third stage – 13:00 UT December 16 to 12:00 UT December 17. This pattern corroborates the findings of Shreve et al. (2019). Both assimilations reveal an intense SO2 degassing event commencing around 23:00 UT on December 14 and concluding at 18:00 UT on December 15. Within this phase, stage 1, the highest gas flux (3.8 kilotonnes per hour ($\mathrm{kt\,h^{-1}}$), denoted as #T2 in Fig. 1a), dated 00:00 UT on December 15, emerges from the TROPOMI data assimilation, coinciding with the eruption's onset linked to the emplacement of a lava flow in the caldera (Shreve et al., 2019). This alignment is substantiated by the rise in the thermal index for lava flow pixels, as derived from the analysis of Himawari-8/AHI observations using the $3.9\,\mu\mathrm{m}$ channel (illustrated by the green line in Fig. 1a). Shreve et al. (2019) demonstrate that the emission of this lava flow coincided with the drainage of Ambrym's long-lived lava lakes. This event occurred on December 14, between 23:20 and 23:40 UT. The TROPOMI-derived SO_2 flux (hourly resolution) and the SO_2 flux proxy (20-minute resolution), which is a qualitative parameter derived from Himawari-8/AHI

observations (indicated by the gray line in Fig. 1a), both peak at the eruption's onset. However, the OMPS data assimilation

220   reveals a much weaker gas pulse ($0.25\,\mathrm{kt\,h^{-1}}$, labeled as #O1 in Fig. 2a) at 00:00 UT 15 December, despite the #O1 emission peaking at 04:00 UT 15 December. The #O1 emission, at $1.8\,\mathrm{kt\,h^{-1}}$, is the second-largest degassing event following #O2, which records $2.0\,\mathrm{kt\,h^{-1}}$. These emissions are identified during the initial phase of the eruption when assimilating OMPS observations. Between 02:00 – 05:00 UT on December 15, TROPOMI-derived SO_2 emissions show another robust degassing event (#T3, Fig. 1a), with a flux reaching up to $2.75\,\mathrm{kt\,h^{-1}}$, albeit with a brief interruption and weaker intensity compared to

225   the eruption's onset. On December 15, between 08:00 and 12:00 UT, there is a notable increase in SO_2 emissions, as detected through the assimilation of TROPOMI (#T4) and OMPS (#O2) data, following a brief interruption. Notably, during the first stage of the eruption, except for the late hours of December 14 (the eruption's onset) and the period between 12:00 – 18:00 UT on December 15, Himawari-8/AHI's SO_2 flux proxy (indicated by the gray line in Fig. 1a) does not indicate significant degassing, in contrast to the findings from both TROPOMI and OMPS data assimilations. This disparity can be attributed

230   to the strong emissions of ash particles expelled simultaneously with SO_2 during that period (as depicted in Fig. S6). The Himawari-8/AHI SO_2 flux proxy is obtained through an analysis of a near-source plume within a roughly $50\,\mathrm{km} \times 35\,\mathrm{km}$ area centered on Ambrym. This analysis uses the $8.5\,\mathrm{\mu m}$ and $10.41\,\mathrm{\mu m}$ channels (Shreve et al., 2019). Consequently, a high concentration of ash in the nearby plume can significantly affect these AHI channels, potentially biasing the SO_2 flux proxy by either underestimating or concealing the presence of SO_2 (e.g., Andres and Schmid, 2001; Surono et al., 2012). In contrast, the

235   flux obtained by assimilating LEO satellite observations, which capture the plume when it has dispersed farther from the source and is more diluted, is less affected by these conditions. In the first stage of the eruption, marked by intense degassing, a clear correlation emerges with high values of the lava flow thermal indices (illustrated by the green line in Fig. 1a). Nevertheless, as the second stage of the eruption commences, these lava flow thermal indices gradually decrease. This observation implies that the lava flow has reached its full extent during the first stage of the eruption, consistent with findings from Sentinel-2 optical

240   images (Shreve et al., 2019). In the subsequent stage, the lava flow continues to emit heat without renewed lava emissions.

During the second stage of the eruption, SO_2 degassing is characterized by the largest peak on December 16, as recorded by TROPOMI-derived flux emissions and Himawari-8/AHI SO_2 flux proxy. From 20:00 UT 15 December to 06:00 UT 16 December, a strong SO_2 flux peaking at $7.1\,\mathrm{kt\,h^{-1}}$ is derived from the TROPOMI data assimilation (#T7 in Fig. 1a), approximately coinciding with the highest values of the SO_2 flux proxy derived from Himawari-8/AHI observations of the eruption (gray line

245   in Fig. 1a). However, the OMPS data assimilation misses this paroxysmal phase, recording degassing activity with an intensity similar to the previous day. Sect. 3.1.2 explains why the discrepancy occurs. Furthermore, as reported by Shreve et al. (2019), a significant earthquake on late December 15 was followed by a sharp rise and lateral migration of seismicity. This suggests that a large volume of magma moved laterally at a shallow depth from the caldera towards the eastern part of the island. Even though this dike, which was over $30\,\mathrm{km}$ long, did not reach the surface and only fractured it, and caused substantial coastal

250   uplift (Shreve et al., 2019). The concomitant paroxysmal phase of degassing that we highlight in the second stage of degassing activity is likely due to the degassing of this voluminous extra-caldera dike.

The third stage, lasting until the end of December 17, has minor degassing, with occasional gas pulses of up to $0.4\,\mathrm{kt\,h^{-1}}$ recorded by TROPOMI and OMPS data assimilations. Himwari-8/AHI-derived proxies show the same degassing pattern.

Ambrym, despite having only three explosive eruptions, was a significant source of passive SO_2 degassing, emitting an esti-
255 mated $122\,\mathrm{kt}$ of SO_2 per year (Carn et al., 2016). Nevertheless, information regarding Ambrym's SO_2 degassing, particularly
in terms of high time resolution and passive emissions, remains scarce. Passive degassing from Ambrym's volcano prior to
the 2018 eruption shows an annual SO_2 mass flux averaging 2–$12\,\mathrm{kt\,d^{-1}}$ (equivalent to 0.08–$0.5\,\mathrm{kt\,h^{-1}}$). This data is derived
from OMI satellite observations spanning from 2005 to 2015, and it has been extended to 2018 using the NASA database (Carn
et al., 2017; Shreve et al., 2022). Additionally, ground-based UV-DOAS observations, which are infrequent due to challenging
260 access, estimate Ambrym's substantial SO_2 passive degassing at $5\,\mathrm{kt\,d^{-1}}$ (equivalent to $0.2\,\mathrm{kt\,h^{-1}}$), aligning with the satellite-
based findings (Bani et al., 2012). Therefore, the SO_2 emissions from Ambrym's passive degassing are significantly lower, by
over one order of magnitude, compared to the estimated degassing rate during its 2018 eruption. Bani et al. (2009) report peak
SO_2 flux values of $33\,\mathrm{kt\,d^{-1}}$ (equivalent to $1.4\,\mathrm{kt\,h^{-1}}$) during intense lava lake degassing in 2005. Our estimation shows that
eruptive SO_2 flux reaches $7.1\,\mathrm{kt\,h^{-1}}$ (emission #T7) during the paroxysmal phase of the 2018 eruption, five times higher than
265 the 2005 lava lake degassing activity. We estimate that the eruption emitted $42 \pm 16\,\mathrm{kt}$ (OMPS) or $52 \pm 13\,\mathrm{kt}$ (TROPOMI) of
SO_2. The additional $10\,\mathrm{kt}$ with TROPOMI corresponds to dense, often young, SO_2 parcels that are more accurately detected,
thanks to its higher spatial resolution compared to OMPS. This budget is consistent with the total SO_2 mass burden of 50–60
kt and 30–40 kt previously estimated for the 2015 and 2018 Ambrym eruptions, respectively (Shreve et al., 2019, 2022). De-
spite its high degassing rate, our estimations show that the 2018 Ambrym eruption released a relatively small amount of SO_2
270 compared to the global sources of eruptive SO_2 emissions, which are about $2000\,\mathrm{kt}$ per year (Carn et al., 2016).

3.1.2 Paroxysmal degassing missed by assimilation of OMPS SO_2 columns

Assimilation of TROPOMI SO_2 columns shows that the highest SO_2 emissions occurred at the end of December 15. This
retrieval agrees with the highest values of the SO_2 flux proxy derived from Himawari-8/AHI observations, offering a 20-
minute temporal resolution (Fig. 1a). We investigate why the strongest SO_2 degassing associated with #T7 and #T8 emissions
275 (Fig. 1a), spanning three ranges of injection heights (3–$5\,\mathrm{km}$, 7–$8\,\mathrm{km}$, with a maximum SO_2 mass of approximately $4\,\mathrm{kt}$ in
10–$12\,\mathrm{km}$, Fig.3a), is largely underestimated by assimilating OMPS observations, which only records about four times weaker
emissions (#O4 in Fig.2a). In the context of OMPS data assimilation, a perplexing situation emerges. It produces the strongest
emission, #O2a (as shown in Fig. 3b and S8b), at approximately 11:00 UT on December 15. In contrast, emissions #O4d
and #O4e (as seen in Fig. S9b) represent the SO_2 plume near the volcano's vicinity at the end of December 15, but they are
280 notably weaker when compared to emission #O2a (as indicated in Fig. S9b, where sources are arranged in descending order by
amplitude). Both TROPOMI and OMPS acquisitions on December 16 display highly concentrated SO_2 parcels near the source
(as revealed in Fig. S12), which pose constraints for retrieving these emissions (#T7e and #T8a in Fig. S9a, #O4d and #O4e in
Fig. S9b) through inverse modeling procedures. To address the discrepancies in the retrievals, we examine SO_2 maps obtained
simultaneously by OMPS and TROPOMI on December 16. Our aim is to determine if differences in the spatial distribution of
285 the plume, as observed by the two sensors, could explain the differences in the retrievals of mass flux and injection altitude at
the source.

On December 16, both OMPS and TROPOMI detect a crescent-shaped SO_2-rich plume emitted by Ambrym that stretches over $1000\,km$ to the east, with a plume core of higher SO_2 density than the periphery (Fig. 4i-1, 4ii-1). TROPOMI detects a highly concentrated SO_2 parcel near the source (#A in Fig. 4ii) and four additional, distinct SO_2-rich parcels at a considerable distance from the source (#B–E in Fig. 4ii). OMPS, by contrast, records no such clear spatial patterns, and only two dense SO_2 parcels near the source are noticeable (Fig. 4i-1). The concentration of these parcels also differs significantly between these two sensors, as shown by plume transects (Fig. 4i-2, 4ii-2). The densest SO_2 parcel identified by TROPOMI (2 pixels) presents a peak column amount value of $664.1\,DU$ (#A in Fig. 4ii-2), while OMPS detects a much less dense parcel, with only one pixel, with a peak value of $30.2\,DU$ (#A in Fig. 4i-2). TROPOMI also indicates another SO_2-rich parcel at a distance of approximately $250\,km$ from the source, with a peak value of $30.5\,DU$ (#B in Fig. 4ii-2), compared to $11.6\,DU$ for OMPS (#B in Fig. 4i-2). TROPOMI measurements also show more pronounced dense SO_2-rich parcels and their fragments with column amounts greater than $10\,DU$ (#C–E in Fig. 4ii-2) than OMPS. TROPOMI's hyperspectral and higher spatial resolution than OMPS explains its ability to detect concentrated areas of SO_2 more effectively (Theys et al., 2019).

To test whether TROPOMI's better spatial resolution explains the differences in the distribution of in-plume SO2 columns between the two sensors, we apply spatial smoothing to TROPOMI data. We smooth TROPOMI column amount pixel observations within a disk with three different radii: $25\,km$ (Fig. 4iii), $50\,km$ (Fig. 4iv), and $75\,km$ (Fig. 4v). As the disk radius increases, the peak SO_2 columns of dense parcels #A to #E within the plume decreases. With a $50\,km$ smoothing, the SO_2 column of parcel #A, the most concentrated parcel, is reduced by 11 times to $59.5\,DU$. The SO_2 columns associated with the four other SO_2-rich parcels farther from the source, ranging from $11\,DU$ to $13\,DU$, are still discernible above a core background of around 7–$8\,DU$. However, with a $75\,km$ smoothing, it becomes difficult to separate these four parcels from the plume core background. Parcel #A is of particular interest because it constrains the strong degassing of the paroxysmal phase (#T7 and #T8, Fig. 1a) in the inverse modeling (see zoomed-in view in Fig. S13). With a $75\,km$ smoothing of TROPOMI data, parcel #A is still discernible, and its concentration peaked at $37.4\,DU$ (Fig. 4v-2), similar to the SO_2 column associated with the same parcel #A in the raw OMPS observations (#A in Fig. 4i-2).

Therefore, TROPOMI data smoothed to a spatial scale of $50\,km$ to $75\,km$ best match raw OMPS data, suggesting that the difference in spatial resolution explains the differences in SO_2 column measurements. TROPOMI's high spatial resolution allows for better characterization of dense SO_2 parcels, especially young highly-concentrated parcels near the source (Fig. S12). This strongly constrains the inverse modeling procedure to retrieve SO_2 mass flux and injection height, resulting in substantially different estimates of flux emissions depending on the satellite measurements. On December 16, emissions #T7e and #T8a (Fig. S9a) clearly indicate a concentrated SO_2 plume near the source. In contrast, emission #O2a (Fig. S9b) does not correspond to the SO_2 plume observed on the same day with a maximum column value of $30.2\,DU$ (Fig. S12). Instead, #O2a is linked to a dense SO_2 parcel situated away from the volcano, injected at an $8\,km$ altitude ASL (Fig. 3b and S9b). This discrepancy raises concerns about the precision of inverse modeling when assimilating low spatial resolution SO_2 images, particularly in capturing dense, localized volcanic SO_2 parcels in the moments leading up to the LEO satellite overpass. Notably, during the paroxysmal phase of the Ambrym eruption at the end of December 15, OMPS data assimilation greatly underestimates SO_2

flux values, with a factor of about 4, as OMPS identifies parcels with concentrations approximately 20 times smaller than those detected by TROPOMI.

3.1.3   A bimodal SO$_2$ injection at eruption onset

Two consecutive LEO satellite images of Ambrym's eruption plume taken on December 15 and 16 between 00:00 and 03:00 UT
325   constrain the inverse modeling to characterize the SO$_2$ injection heights at the eruption onset, which took place late December 14 (around 23:40 UT). On December 15 at 00:00 UT, TROPOMI and OMPS SO$_2$ column assimilations reveal that Ambrym volcano emitted SO$_2$ at two distinct altitude ranges, resulting in a bimodal vertical distribution. The most substantial emissions occurred between 9–11 km ASL, with a secondary emission layer at 4–5 km ASL, corresponding to emissions labeled #T2a–c and #O1a—c in Fig. 3. Every 20 minutes, SO$_2$ RGB composites from Himawari-8/AHI observations show the SO$_2$ plume
330   progressively separating into two distinct branches starting from 01:00 UT on December 15 (left column of Fig. 5, animation M1, and Fig. S6 for longer time series). This separation affirms that SO$_2$ is injected at various levels early in the eruption, ascending to 9–11 km ASL. In contrast, ash remained at lower altitudes due to wind shear. The result is a complex plume shape with distinct branches dispersing at different altitudes. The HYSPLIT Lagrangian model (Stein et al., 2015), forced by 0.5-degree GDAS reanalysis, shows that releasing ash particles at 00:00 UT on December 15 at an altitude of 5 km ASL (Fig.
335   5-vii) reproduces one branch of the plume moving north-northeast, which is likely the ash branch observed by Himawari-8/AHI (Fig. 5iv–5vi). Releasing SO$_2$ at higher altitudes (Fig. 5-viii, 5-ix) fits well with the spatial extent and direction of the SO$_2$ plume indicated by the light greenish plume in the SO$_2$ RGB composites from Himawari-8/AHI observations.

3.1.4   Pre-eruptive degassing

Around 15:00 UT on December 14, TROPOMI data assimilation reveals an above-noise-level SO$_2$ emission (#T1, as shown
340   in Fig. 1a) at an altitude of 11 km ASL, with a mass-flux of up to 1.0 kt h^{-1} (Fig. 3a). However, the OMPS data assimilation fails to detect this emission (Fig. 3b). This emission occurs nearly 12 hours before the satellite overpass and 8 hours before the release of the strong SO$_2$ emission (#T2) associated with the eruption onset is expelled. Furthermore, the Himawari-8/AHI SO$_2$ RGB images do not indicate the presence of the SO$_2$ plume near the source at this particular time (see animation M1).

We find that the SO$_2$ emission #T1 is constrained by the presence of dense SO$_2$ pixels detected near 175° E on December
345   15, even in the noisy swath edge (Fig. 1b-ii and Fig. S14a-ii for a closer view). This scenario poses challenges as it involves modeling emission parameters using weak but mostly above-noise SO$_2$ columns. Such complexities arise when the volcanic plume is positioned at the swath's edge, where noise levels are higher compared to other pixels. This challenging situation is encountered on multiple occasions, with the same pixels appearing at the swath's edge on the previous day, December 14 (Fig. S12 and Fig. S14a-i). Notably, emission #T1 remains visible on December 16, forming the forefront of the plume (Fig.
350   S14d-iii), even in the presence of cloud interference (Fig. 7a-iii). Conversely, this pre-eruptive degassing cannot be retrieved through the assimilation of OMPS data due to increased noise and distortion in the coarser OMPS pixels at the swath's edge (Fig. S14b). The Himawari-8/AHI SO$_2$ RGB images, less sensitive to weak emissions, do not show any SO$_2$ plume near the source at 15:00 UT on December 14 (see animation M1). Nevertheless, volcano-seismic activity began at Ambrym between

13:00 – 20:00 UT (local nighttime) on December 14, with a small increase in lava flow activity (Shreve et al., 2019), which
355 could have been accompanied by weak degassing. The available SO_2 data do not provide sufficient constraints for the inverse
modeling procedures to determine the injection height of the #T1 emission. This is shown in the gray contour in Fig. 3a, along
with retrievals that have uncertainties concerning injection heights. It is improbable for weak SO_2 degassing (#T1) to reach
11 km ASL. Sect. 4.2 provides more information about the uncertainty of SO_2 injection heights related to weak flux values.

3.2 Locating SO_2 plumes beneath clouds: Performance of inverse modeling in mitigating satellite retrieval limitations

360 Satellites, especially those with LEO sensors, have difficulty detecting SO_2 plumes in cloudy areas (e.g., Carn et al., 2013),
but our inverse modeling procedure overcomes this challenge by assimilating highly sensitive SO_2 data from TROPOMI. Our
procedure successfully simulates the presence of SO_2 plumes in cloudy areas by assimilating successive satellite overpass data
of volcanic SO_2 plumes, even when some images are obscured by clouds.

Figs. 1 and 2 show that initializing the CHIMERE CTM simulation with inverted SO_2 emissions results in an elongated
365 SO_2 plume forming to the north-northeast of Ambrym, mainly on December 17 and 18. Both sensors encounter difficulty
in detecting the plume, yet faint SO_2 signals are visible in TROPOMI observations, as depicted by the red contoured areas
in Fig. 6ii. Using TROPOMI-derived SO_2 emissions to initialize the CTM simulation reduces the presence of the simulated
SO_2 plume, especially to the northeast of Ambrym, with the application of a cloud fraction threshold (set at 0.3 to indicate
significant cloud cover). Similarly, the CTM simulation, initialized with SO_2 emissions from OMPS data assimilation, extends
370 the plume to north-northeastern regions near the source. However, OMPS is unable to detect volcanic SO_2 plumes obscured
by clouds (Fig. 6i), rendering this simulated SO_2 plume extension unreliable. Consequently, this cloud fraction threshold lacks
conclusive applicability in OMPS data assimilation. TROPOMI's improved spatial resolution confirms the plume's presence
in cloudy regions, underscoring the potential for our inverse modeling procedure to assimilate TROPOMI data. This procedure
integrates cloud-free TROPOMI observations of the SO_2 plume from previous days and offers a promising method for modeling
375 concealed SO_2 plumes. However, we must also acknowledge the limits of this procedure. The procedure may be less effective
when the SO_2 plume remains entirely concealed by clouds for an extended duration spanning multiple days during the satellite
overpass.

4 Discussion

4.1 Temporal resolution of SO_2 flux

380 The week-long eruption of Ambrym exhibits distinct patterns in SO_2 emissions in three stages (Fig. 1a). TROPOMI data
assimilation reveals ten discernible peaks labeled as #T1 to #T10 in SO_2 flux time series, while OMPS data assimilation
produces only six peaks, labeled as #O1 to #O6. In Fig. 2a, we observe the absence of two prominent peaks in the SO_2 flux
time series derived from OMPS data assimilation during the early hours of December 16. On December 15, during the initial
stage of the eruption (stage 1), the assimilation of OMPS data produces a visibly smoothed representation of the time evolution

385 of SO$_2$ emissions, identified as #O1. This stands in contrast to the dynamically varying #T2 and #T3 peaks evident in the TROPOMI-derived SO$_2$ flux time series. The fluctuation in TROPOMI-derived SO$_2$ flux indicates its capability to detect short-lived SO$_2$ emissions, owing to its capability of measuring SO$_2$ at high spatial resolution. It is important to recognize that the effectiveness of the inverse modeling procedure relies on the accurate simulation of local wind shears by the CTM. Following the paroxysmal phase of the eruption (stage 3), both time series for SO$_2$ flux eventually converge to exhibit similar behavior

390 during the final stage of quiescent degassing. To establish convergence between these two SO$_2$ flux time series, we use a simple moving average (SMA) with a 2- to 8-hour window on the TROPOMI-inverted SO$_2$ flux time series. Our analysis reveals that when using a 7–8 hour SMA window, TROPOMI-derived SO$_2$ flux closely aligns with OMPS-derived SO$_2$ flux, exhibiting a strong correlation coefficient of 0.77 (Fig. 7d). Note that the correlation coefficient between OMPS-derived SO$_2$ flux time series and unsmoothed flux from assimilating TROPOMI observations decreases to 0.55. This decrease in the correlation

395 coefficient is mainly because OMPS cannot accurately measure SO$_2$ emissions during the initial (stage 1) and paroxysmal (stage 2) eruption phases, as reported in sect. 3.1. As a result, assimilating TROPOMI observations into CHIMERE CTM produces a more dependable time series of SO$_2$ flux with improved temporal resolution. This procedure effectively captures short-lived and intense pulses of SO$_2$ emissions. In summary, assimilating high spatial resolution SO$_2$ column observations leads to the retrieval of high temporal resolution SO$_2$ emissions.

400 ## 4.2 Limitations of the inverse modeling procedure

4.2.1 Modeling emissions over time

The CTM simulation, initialized with inverted SO$_2$ sources, closely aligns with LEO satellite observations, maintaining a mean residual close to zero in the normal distribution throughout the entire eruption period (Fig. S15). However, the increased standard deviation of analysis residuals, primarily on December 16 (Fig. S15d, S15g), highlights the limitations of inverse

405 modeling. On December 16, the CTM simulation does not fully replicate the leading forefront of the plume, as shown in Fig. 1c and S16. Additionally, it faces challenges in distinguishing between the two branches of the SO$_2$ plume over the Fiji and Vanuatu islands on December 17 (Fig. 1d, 2d).

The wind fields in the CTM simulation may lack vertical mixing and horizontal shears. The simulation may have also removed most of the emissions by a false precipitation event, or transport errors may have accumulated over time, adding

410 biases to the aged plume. This deficiency could stem from either the resolution of the forcing WRF meteorological model or the quality of the archived reanalysis data, affecting the trajectory accuracy of plume parcels, particularly for distant or aged tracers (see Boichu et al., 2013). To mitigate this uncertainty, we need to limit the ingestion of excessively distant or aged plume sections into the inversion procedures. Furthermore, the CTM simulation cannot replicate concentrated SO$_2$ parcels near the source. This is because of a well-known issue in Eulerian CTMs, where there is excessive diffusion, as discussed by Freitas

415 et al. (2012). This discrepancy is the cause of the high standard deviation in analysis residuals observed on December 15 (Fig. S15c-iv) and 16 (Fig. S15d-iv). Specifically, the CTM simulation, initialized with TROPOMI-derived SO$_2$ emissions, cannot generate the dense SO$_2$ columns measured by TROPOMI near the source. Notably, this problem does not occur when the CTM

simulation is initialized with OMPS-derived SO_2 sources. In addition, observational data indicates that meteorological clouds have a substantial impact on the detection of satellite SO_2 plumes on December 17 and 18 (Fig. 6). In Fig. S17, we present a

420 schematic depicting such scenarios in which the inversion procedure for SO_2 emission profiles is affected by bias resulting from less observational constraint or inherent bias in the CTM simulation. Despite all these challenges, thanks to the assimilation of multiple successive satellite overpass images of the dispersed SO_2 plume, the CHIMERE CTM simulation could reasonably produce SO_2-rich parcels across this continental-scale domain (sect. 3.1).

4.2.2 Overestimating the altitude of SO_2 emissions linked to weak flux emissions

425 In our inverse modeling procedure, we employ a sifting threshold, detailed in Fig. S5 and described in section 2.4, to detect and filter out SO_2 emissions obtained through the data assimilation with significant uncertainty. Despite this, we still encounter emissions that exhibit conflicting attributes, notably low flux values and unexpectedly high injection altitudes, occurring in the initial and third stages of the eruption (indicated in gray contours Fig. 3). For example, the pre-eruptive emission #T1 (contoured in gray in Fig. 3a) with an amplitude of $1 \, \mathrm{kt \, h^{-1}}$ is injected at an altitude of $11 \, \mathrm{km}$ ASL. SO_2 plume linked to this

430 emission aligns with the leading edge of the plume on December 15 (Fig. S14a) but falls within the LEO satellite swath's edge, where both sensors have difficulty in detecting SO_2 plume (sect. 3.1.4). Moreover, on December 16, this emission contributes to the northern segment of the main SO_2 plume (Fig. S14d-iii), remaining undetected by the LEO satellites due to meteorological clouds (red contoured lines in Fig. 6a).

In a broader context, we observe that the low SO_2 emissions with large uncertainty, which are subsequently filtered out

435 during the post-processing of inverse modeling results (sect. 2.4), tend to reach higher injection altitudes (Fig. S5). These emissions typically register at less than $0.5 \, \mathrm{kt \, h^{-1}}$ flux values, considered as the background level, but they tend to be released at an average altitude higher than $6 \, \mathrm{km}$ ASL. Concerning TROPOMI-derived SO_2 flux, these exclude SO_2 emissions amounting to $13 \, \mathrm{kt}$ of SO_2 mass, while for OMPS-derived SO_2 flux, the total is $16 \, \mathrm{kt}$ (Fig. S5). OMPS data assimilation rejects more SO_2 mass than TROPOMI data assimilation, even when the sifting threshold is the same. This is because OMPS is less sensitive to

440 weak emissions.

Stohl et al. (2011) report a tendency for volcanic emission source terms derived from inverse modeling to shift towards higher altitudes when extracting ash injection heights from the 2010 Icelandic eruption. They attribute this behavior to systematic errors in satellite detection and disparities with a priori emission knowledge that do not align with satellite measurements. Their Lagrangian transport model simulation resolution is more than 7 times coarser than ours, and they identify continuous

445 emissions at approximately 10–$11 \, \mathrm{km}$ ASL throughout their study period. There are two key explanations for these types of SO_2 emission retrievals by inverse modeling. Firstly, weak emissions from point sources like volcanoes are challenging to detect via satellites, providing limited constraints for inverse modeling. Additionally, the presence of meteorological clouds can hinder the detection of dense SO_2 plumes, falsely rendering them as weak SO_2 columns in LEO satellite images (see red contoured regions in Fig. 6-ii). TROPOMI's high spatial resolution proves invaluable in addressing this issue, as demonstrated

450 in our pre-eruption SO_2 emission analysis (as shown in gray contours in Fig. 3a). Secondly, the tendency for these retrievals to be associated with higher altitudes can be explained from a modeling perspective. Tracers released at higher altitudes disperse

more quickly due to larger wind fields, particularly within the planetary boundary layer and troposphere (as demonstrated by Stoffelen et al. (2005)). This leads to faster and wider spatial dispersion, resulting in lower SO_2 molecule density per unit area compared to emissions at lower altitudes. In contrast, lower altitudes with weaker wind fields maintain a higher SO_2 molecule density per unit area, which contradicts the satellite observations of weak SO_2 columns. This discrepancy means that the weak SO_2 columns observed by satellites are less likely to correspond to low-altitude tracer emissions, especially in the context of the linear least-squares optimization procedure. This challenge is further exacerbated in OMPS data assimilation due to its coarser spatial resolution.

Inverse modeling of weak SO_2 columns is indeed challenging, but employing higher-resolution satellite observations, such as TROPOMI, greatly aids in accurately capturing emission timing. However, precise determination of the injection height for these uncertain emissions is vital, constrained by sensor sensitivity limitations and daily observations. Therefore, the interpretation of such emissions, highlighted in gray in Fig. 3, requires caution. In such situations, SO_2 height products like IASI SO_2 height products (Clarisse et al., 2014) or TROPOMI SO_2 height products (Hedelt et al., 2019) become crucial in constraining the inverse modeling procedure.

4.3 Insights into volcanological processes

Following an initial moderate magma intrusion resulting in surface activity within the caldera and a lava flow, a substantial magma-filled dike was intruded at a shallow depth. This dike caused significant deformation of the island, as documented by Shreve et al. (2019, 2022). The dike's propagation towards the eastern part of the island led to a surface rupture and ultimately triggered a submarine eruption offshore.

During the first stage of the eruption, we observe a significant correlation between the thermal activity of the lava flow, indicated by the thermal index of lava flow pixels from Himawari-8/AHI observations (green line in Fig. 1a), and the TROPOMI-inverted SO_2 flux time series (red line in Fig. 1a). Emissions labeled #T2 and #T3 coincide with an increase in lava flow activity on December 15, between 00:30 and 04:30 UT, as documented by Shreve et al. (2019). Emission #T2 reaches altitudes between 9–10 km ASL, discharging approximately 3.5 kt of SO_2. Meanwhile, emission #T3 releases about 3.5 kt of SO_2 at an altitude of 5 km, along with an additional 0.5 kt at 2 km ASL. Emissions labeled #T4 and #T5, preceding a significant seismic event around 20:00 UT on December 15 (Shreve et al., 2019), also coincide with the lava flow, indicating that the primary source of SO_2 degassing during this phase is closely related to the degassing of the spreading lava flow within the caldera.

At the onset of the second stage of the eruption on December 16, there is a notable shift in eruption dynamics. During this period, the thermal activity within the intra-caldera lava flow returns to a pre-eruptive background level, indicating the cessation of lava emission, as confirmed by Sentinel-2 images in Shreve et al. (2019). It suggests that the lava flow has reached its full extent. However, the TROPOMI-derived SO_2 flux reveals a sudden, substantial increase in SO_2 emissions (#T7 and #T8), releasing over 10 kt of SO_2 and reaching heights of approximately 11 km ASL (Fig. 3a). This increase is associated with the most significant paroxysmal degassing event since the onset of the eruption. It occurs shortly after a renewed seismic activity, as reported by Shreve et al. (2019), supporting the intrusion of a substantial dike that propagates towards the eastern part of

485   the island. Consequently, the heightened degassing on December 16 likely results from gases originating from the voluminous dike intrusion, which separated from the magma and reached the surface as the dike propagated at a depth of a few kilometers.

Therefore, the assimilation of TROPOMI observations enables the retrieval of hourly-resolved SO_2 emissions. This procedure not only facilitates the monitoring of changes in eruptive dynamics but also aids in identifying various magma sources of SO_2 emission. Additionally, it offers an advantage over Himawari-8/AHI observations by being less affected by ash co-

490   emission. The high temporal resolution provided by LEO satellite data assimilation serves as an additional resource for supporting local volcanological observatories in their efforts to assess local hazards.

5   Conclusions

Our inverse modeling procedure, applied to the 2018 Ambrym eruption, reveals significant benefits from assimilating TROPOMI's hyperspectral and high-spatial resolution SO_2 column measurements, providing valuable insights into the different phases of

495   magma degassing. The assimilation of TROPOMI data excels at capturing short-lived SO_2 emissions. This capability is attributed to TROPOMI's high spatial resolution, allowing it to detect young and narrow plume fragments. This precision significantly improves the accuracy of estimating high SO_2 flux values, especially during the paroxysmal phase of the eruption. Furthermore, TROPOMI data assimilation demonstrates heightened sensitivity to weak pre-eruptive fluxes, even in areas where measured pixels fall within noisy swath edges. This results in a higher-resolution SO_2 flux time series that remains unimpacted

500   by ash co-emissions. It serves as a valuable complement to geostationary satellite measurements, which can miss the SO_2 flux proxy during ash co-emission phases. Our inverse modeling procedure further demonstrates the feasibility of predicting the presence of SO_2 plumes below meteorological clouds by assimilating successive images of dispersed SO_2 plumes, especially assimilating the more sensitive TROPOMI observations. Lastly, our findings shed light on the origins of the Ambrym eruption's SO_2 degassing, which stems from two distinct magma sources. One is associated with surface-level lava flow activity,

505   while the other involves the substantial degassing of SO_2 during the paroxysmal phase of the eruption, originating from a voluminous magma intrusion at shallow depths. The total SO_2 emission budget of this eruption is 42 ± 16 kt (OMPS) or 52 ± 13 kt (TROPOMI), surprisingly unaffected by the voluminous magma accumulation ($>0.4 \, km^3$) at shallow depth that fractured the surface until the eastern coast.

To enhance the accuracy of SO_2 mass flux and injection height retrieved through inverse modeling procedure, reducing

510   the time lag between emissions and data acquisition is fundamental. Additionally, assimilating observations with varying sensitivities to SO_2 altitude and coexisting particles in volcanic plumes would enhance the accuracy of the retrieved source emissions. Our future plans involve assimilating hyperspectral SO_2 column observations from both UV and IR satellite sensors, harnessing their respective strengths. IR sensors, such as IASI, provide a distinct sensitivity to ash particles and acquire data bi-daily, encompassing both day and night, unlike UV satellite sensors that offer daily observations. Additionally, the assimilation

515   of SO_2 height data from IR sensors in the inverse modeling procedure is expected to enhance the accuracy of emission profiles.

Code availability. The CHIMERE CTM code (version: 2017r4), used in this study, can be accessed for free at the LMD laboratory repository in Paris, France (https://www.lmd.polytechnique.fr/chimere/). Similarly, the WRF-ARW model code used in the simulation (version: 4.1.3) can be found on the Git-Hub platform (https://github.com/wrf-model). These simulations were performed on the LOA HPC facilities using INTEL-licensed libraries, including the Intel version 2020.1.217 and the Intel MPI version 2019.7.217. Other software packages used include
520 the HDF5 library (version: 1.12.1), NetCDF4 library from Unidata (version: 4.8.1), and PnetCDF library from Argonne laboratory (version: 1.12.3). The preparation of the Jacobian matrix, a key component in the inverse modeling procedure, was carried out using Python (version 3.10.9) modules, along with CDO (version: 2.1.1) and NCO (version: 5.1.4) python bindings. Most of the figures are created using the Generic Mapping Tool (GMT) libraries (version: 6.3.0), and a few are prepared using Matplotlib (version: 3.6.3). Inkscape version 1.2.2 is used to arrange the individual figures in the panels.

525 *Data availability.* The ERA-5 reanalysis data used to drive the WRF run are available for free on the climate data store of ECMWF (https://cds.climate.copernicus.eu/cdsapp#!/home). TROPOMI and OMPS SO_2 columns (level 2) are obtained from the NASA GES DISC platform (https://disc.gsfc.nasa.gov/).

Video supplement. Throughout December 13–18, 2018, geostationary Himawari-8's SO_2 RGB composite images are made available for viewing the SO_2 emissions from Ambrym every 20 minutes.

530 *Author contributions.* The original idea was conceived by MB. The inverse modeling setup was developed, and remote sensing data were obtained by MB, AKB, and FT. AKB and FT conducted the numerical calculations. NH and SH prepared and analyzed the Himawari-8/AHI data. The results were examined by AKB, MB, and SH. AKB wrote the manuscript, which was reviewed, commented on, and revised by MB and SH. All authors approved the article.

Competing interests. The authors declare that they have no conflict of interest.

535 *Acknowledgements.* This study received support from the ANR VOLCPLUME project (ANR-15-CE04-0003), Labex Cappa, and CLimiBio projects at Univ. Lille. We used TROPOMI and OMPS nadir-viewing SO2 observations from NASA GES DISC. The numerical calculations were performed on the HPC platform at LOA CNRS UMR 8518 in a licensed Intel environment (version 2020). Special thanks to the VOLCPLUME portal hosted by AERIS/ICARE Data and Service Center for facilitating our assessment of Himawari-8/AHI SO2 and ash RGB composite images, cloud top altitude, and brightness temperatures.

References

Allibone, R., Cronin, S. J., Charley, D. T., Neall, V. E., Stewart, R. B., and Oppenheimer, C.: Dental fluorosis linked to degassing of Ambrym volcano, Vanuatu: a novel exposure pathway, Environmental Geochemistry and Health, 34, 155–170, https://doi.org/10.1007/s10653-010-9338-2, 2012.

Andres, R. and Schmid, J.: The effects of volcanic ash on COSPEC measurements, Journal of Volcanology and Geothermal Research, 108, 237–244, 2001.

Arellano, S., Galle, B., Apaza, F., Avard, G., Barrington, C., Bobrowski, N., Bucarey, C., Burbano, V., Burton, M., Chacón, Z., et al.: Synoptic analysis of a decade of daily measurements of SO 2 emission in the troposphere from volcanoes of the global ground-based Network for Observation of Volcanic and Atmospheric Change, Earth System Science Data, 13, 1167–1188, 2021.

Bani, P., Oppenheimer, C., Varekamp, J. C., Quinou, T., Lardy, M., and Carn, S.: Remarkable geochemical changes and degassing at Voui crater lake, Ambae volcano, Vanuatu, Journal of Volcanology and Geothermal Research, 188, 347–357, 2009.

Bani, P., Oppenheimer, C., Allard, P., Shinohara, H., Tsanev, V., Carn, S., Lardy, M., and Garaebiti, E.: First estimate of volcanic SO_2 budget for Vanuatu island arc, Journal of Volcanology and Geothermal Research, 211, 36–46, 2012.

Beirle, S., Hörmann, C., Penning de Vries, M., Dörner, S., Kern, C., and Wagner, T.: Estimating the volcanic emission rate and atmospheric lifetime of SO$_2$ from space: a case study for Kīlauea volcano, Hawai'i, Atmospheric Chemistry and Physics, 14, 8309–8322, https://doi.org/10.5194/acp-14-8309-2014, 2014.

Bessho, K., Date, K., Hayashi, M., Ikeda, A., Imai, T., Inoue, H., Kumagai, Y., Miyakawa, T., Murata, H., Ohno, T., et al.: An introduction to Himawari-8/9—Japan's new-generation geostationary meteorological satellites, Journal of the Meteorological Society of Japan. Ser. II, 94, 151–183, 2016.

Bey, I., Jacob, D. J., Yantosca, R. M., Logan, J. A., Field, B. D., Fiore, A. M., Li, Q., Liu, H. Y., Mickley, L. J., and Schultz, M. G.: Global modeling of tropospheric chemistry with assimilated meteorology: Model description and evaluation, Journal of Geophysical Research: Atmospheres, 106, 23 073–23 095, 2001.

Boichu, M. and Mathurin, T.: VOLCPLUME PORTAL, https://www.icare.univ-lille.fr/volcplume/, https://doi.org/https://doi.org/10.25326/362, 2022.

Boichu, M., Menut, L., Khvorostyanov, D., Clarisse, L., Clerbaux, C., Turquety, S., and Coheur, P.-F.: Inverting for volcanic SO$_2$ flux at high temporal resolution using spaceborne plume imagery and chemistry-transport modelling: the 2010 Eyjafjallajökull eruption case-study, Atmospheric Chemistry and Physics, 13, 8569–8584, 2013.

Boichu, M., Clarisse, L., Khvorostyanov, D., and Clerbaux, C.: Improving volcanic sulfur dioxide cloud dispersal forecasts by progressive assimilation of satellite observations, Geophysical research letters, 41, 2637–2643, 2014.

Boichu, M., Clarisse, L., Péré, J.-C., Herbin, H., Goloub, P., Thieuleux, F., Ducos, F., Clerbaux, C., and Tanré, D.: Temporal variations of flux and altitude of sulfur dioxide emissions during volcanic eruptions: implications for long-range dispersal of volcanic clouds, Atmospheric Chemistry and Physics, 15, 8381–8400, 2015.

Boichu, M., Chiapello, I., Brogniez, C., Péré, J.-C., Thieuleux, F., Torres, B., Blarel, L., Mortier, A., Podvin, T., Goloub, P., et al.: Current challenges in modelling far-range air pollution induced by the 2014–2015 Bárðarbunga fissure eruption (Iceland), Atmospheric Chemistry and Physics, 16, 10 831–10 845, 2016.

575   Boichu, M., Favez, O., Riffault, V., Petit, J.-E., Zhang, Y., Brogniez, C., Sciare, J., Chiapello, I., Clarisse, L., Zhang, S., et al.: Large-scale particulate air pollution and chemical fingerprint of volcanic sulfate aerosols from the 2014–2015 Holuhraun flood lava eruption of Bárðarbunga volcano (Iceland), Atmospheric Chemistry and Physics, 19, 14 253–14 287, 2019.

Cai, Z., Griessbach, S., and Hoffmann, L.: Improved estimation of volcanic SO2 injections from satellite retrievals and Lagrangian transport simulations: the 2019 Raikoke eruption, Atmos. Chem. Phys., 22, 6787–6809, https://doi.org/10.5194/acp-22-6787-2022, 2022.

580   Campion, R., Martinez-Cruz, M., Lecocq, T., Caudron, C., Pacheco, J., Pinardi, G., Hermans, C., Carn, S., and Bernard, A.: Space- and ground-based measurements of sulphur dioxide emissions from Turrialba Volcano (Costa Rica), Bulletin of Volcanology, 74, 1757–1770, https://doi.org/10.1007/s00445-012-0631-z, 2012.

Carn, S., Krotkov, N., Yang, K., and Krueger, A.: Measuring global volcanic degassing with the Ozone Monitoring Instrument (OMI), Geological Society, London, Special Publications, 380, 229–257, 2013.

585   Carn, S., Yang, K., Prata, A., and Krotkov, N.: Extending the long-term record of volcanic SO_2 emissions with the Ozone Mapping and Profiler Suite nadir mapper, Geophysical Research Letters, 42, 925–932, 2015.

Carn, S., Clarisse, L., and Prata, A. J.: Multi-decadal satellite measurements of global volcanic degassing, Journal of Volcanology and Geothermal Research, 311, 99–134, 2016.

Carn, S., Fioletov, V., McLinden, C., Li, C., and Krotkov, N.: A decade of global volcanic SO2 emissions measured from space, Scientific

590   reports, 7, 1–12, 2017.

Carn, S. A. and Bluth, G. J. S.: Prodigious sulfur dioxide emissions from Nyamuragira volcano, D.R. Congo, Geophysical Research Letters, 30, https://doi.org/https://doi.org/10.1029/2003GL018465, 2003.

Carn, S. A., Krueger, A. J., Krotkov, N. A., Yang, K., and Evans, K.: Tracking volcanic sulfur dioxide clouds for aviation hazard mitigation, Natural Hazards, 51, 325–343, 2009.

595   Clarisse, L., Coheur, P.-F., Theys, N., Hurtmans, D., and Clerbaux, C.: The 2011 Nabro eruption, a SO_2 plume height analysis using IASI measurements, Atmospheric chemistry and physics, 14, 3095–3111, 2014.

Copernicus Sentinel data processed by ESA, G. A. C. D.: TROPOMI Level 2 Sulphur Dioxide, 10.5270/S5P-yr8kdpp, https://doi.org/10.5270/s5p-74eidii, 2020.

Corradini, S., Guerrieri, L., Brenot, H., Clarisse, L., Merucci, L., Pardini, F., Prata, A. J., Realmuto, V. J., Stelitano, D., and Theys,

600   N.: Tropospheric Volcanic SO2 Mass and Flux Retrievals from Satellite. The Etna December 2018 Eruption, Remote Sensing, 13, https://doi.org/10.3390/rs13112225, 2021.

Cronin, S. J. and Sharp, D. S.: Environmental impacts on health from continuous volcanic activity at Yasur (Tanna) and Ambrym, Vanuatu, International Journal of Environmental Health Research, 12, 109–123, 2002.

Delmelle, P., Stix, J., Baxter, P., Garcia-Alvarez, J., and Barquero, J.: Atmospheric dispersion, environmental effects and potential

605   health hazard associated with the low-altitude gas plume of Masaya volcano, Nicaragua, Bulletin of Volcanology, 64, 423–434, https://doi.org/10.1007/s00445-002-0221-6, 2002.

Demmel, J. W.: The geometry of Ill-conditioning, Journal of Complexity, 3, 201–229, https://doi.org/https://doi.org/10.1016/0885-064X(87)90027-6, 1987.

Eckhardt, S., Prata, A., Seibert, P., Stebel, K., and Stohl, A.: Estimation of the vertical profile of sulfur dioxide injection into the atmosphere

610   by a volcanic eruption using satellite column measurements and inverse transport modeling, Atmospheric Chemistry and Physics, 8, 3881–3897, 2008.

Edmonds, M., Oppenheimer, C., Pyle, D., Herd, R., and Thompson, G.: SO2 emissions from Soufrière Hills Volcano and their relationship to conduit permeability, hydrothermal interaction and degassing regime, Journal of Volcanology and Geothermal Research, 124, 23–43, https://doi.org/https://doi.org/10.1016/S0377-0273(03)00041-6, 2003.

615 Eskes, H. and Boersma, K.: Averaging kernels for DOAS total-column satellite retrievals, Atmospheric Chemistry and Physics, 3, 1285–1291, 2003.

Esse, B., Burton, M., Hayer, C., Contreras-Arratia, R., Christopher, T., Joseph, E. P., Varnam, M., and Johnson, C.: SO2 emissions during the 2021 eruption of La Soufrière, St Vincent, revealed with back-trajectory analysis of TROPOMI imagery, Geological Society, London, Special Publications, 539, SP539–2022–77, https://doi.org/10.1144/SP539-2022-77, 2023.

620 Feng, M., Duan, Y., Wijffels, S., Hsu, J.-Y., Li, C., Wang, H., Yang, Y., Shen, H., Liu, J., Ning, C., et al.: Tracking air–sea exchange and upper-ocean variability in the Indonesian–Australian Basin during the onset of the 2018/19 Australian summer monsoon, Bulletin of the American Meteorological Society, 101, E1397–E1412, 2020.

Fioletov, V., McLinden, C. A., Kharol, S. K., Krotkov, N. A., Li, C., Joiner, J., Moran, M. D., Vet, R., Visschedijk, A. J. H., and Denier van der Gon, H. A. C.: Multi-source SO2 emission retrievals and consistency of satellite and surface measurements with reported emissions, 625 Atmos. Chem. Phys., 17, 12 597–12 616, https://doi.org/10.5194/acp-17-12597-2017, 2017.

Fioletov, V., McLinden, C. A., Griffin, D., Theys, N., Loyola, D. G., Hedelt, P., Krotkov, N. A., and Li, C.: Anthropogenic and volcanic point source SO 2 emissions derived from TROPOMI on board Sentinel-5 Precursor: first results, Atmospheric Chemistry and Physics, 20, 5591–5607, 2020.

Fioletov, V. E., McLinden, C. A., Krotkov, N., Li, C., Joiner, J., Theys, N., Carn, S., and Moran, M. D.: A global catalogue of large SO$_2$ 630 sources and emissions derived from the Ozone Monitoring Instrument, Atmospheric Chemistry and Physics, 16, 11 497–11 519, 2016.

Fioletov, V. E., McLinden, C. A., Griffin, D., Abboud, I., Krotkov, N., Leonard, P. J. T., Li, C., Joiner, J., Theys, N., and Carn, S.: Version 2 of the global catalogue of large anthropogenic and volcanic SO$_2$ sources and emissions derived from satellite measurements, Earth System Science Data, 15, 75–93, https://doi.org/10.5194/essd-15-75-2023, 2023.

Flemming, J. and Inness, A.: Volcanic sulfur dioxide plume forecasts based on UV satellite retrievals for the 2011 635 Grímsvötn and the 2010 Eyjafjallajökull eruption, Journal of Geophysical Research: Atmospheres, 118, 10,172–10,189, https://doi.org/https://doi.org/10.1002/jgrd.50753, 2013.

Flynn, L., Long, C., Wu, X., Evans, R., Beck, C., Petropavlovskikh, I., McConville, G., Yu, W., Zhang, Z., Niu, J., et al.: Performance of the ozone mapping and profiler suite (OMPS) products, Journal of Geophysical Research: Atmospheres, 119, 6181–6195, 2014.

Flynn, L. E., Seftor, C. J., Larsen, J. C., and Xu, P.: The ozone mapping and profiler suite, in: Earth science satellite remote sensing, pp. 640 279–296, Springer, 2006.

Freitas, S. R., Rodrigues, L. F., Longo, K. M., and Panetta, J.: Impact of a monotonic advection scheme with low numerical diffusion on transport modeling of emissions from biomass burning, Journal of Advances in Modeling Earth Systems, 4, 2012.

Guffanti, M., Casadevall, T. J., and Budding, K. E.: Encounters of aircraft with volcanic ash clouds: A compilation of known incidents, 1953-2009, US Department of Interior, US Geological Survey, 2010a.

645 Guffanti, M., Schneider, D. J., Wallace, K. L., Hall, T., Bensimon, D. R., and Salinas, L. J.: Aviation response to a widely dispersed volcanic ash and gas cloud from the August 2008 eruption of Kasatochi, Alaska, USA, Journal of Geophysical Research: Atmospheres, 115, https://doi.org/https://doi.org/10.1029/2010JD013868, 2010b.

Hamling, I. J., Cevuard, S., and Garaebiti, E.: Large-Scale Drainage of a Complex Magmatic System: Observations From the 2018 Eruption of Ambrym Volcano, Vanuatu, Geophysical Research Letters, 46, 4609–4617, 2019.

650 Hansell, A. and Oppenheimer, C.: Health Hazards from Volcanic Gases: A Systematic Literature Review, Archives of Environmental Health: An International Journal, 59, 628–639, https://doi.org/10.1080/00039890409602947, 2004.

Hansen, P. C.: Rank-deficient and discrete ill-posed problems: numerical aspects of linear inversion, SIAM, 1998.

Hansen, P. C. and O'Leary, D. P.: The Use of the L-Curve in the Regularization of Discrete Ill-Posed Problems, SIAM Journal on Scientific Computing, 14, 1487–1503, https://doi.org/10.1137/0914086, 1993.

655 Hedelt, P., Efremenko, D. S., Loyola, D. G., Spurr, R., and Clarisse, L.: Sulfur dioxide layer height retrieval from Sentinel-5 Precursor/TROPOMI using FP_ILM, Atmospheric Measurement Techniques, 12, 5503–5517, 2019.

Heng, Y., Hoffmann, L., Griessbach, S., Rößler, T., and Stein, O.: Inverse transport modeling of volcanic sulfur dioxide emissions using large-scale simulations, Geoscientific Model Development, 9, 1627–1645, https://doi.org/10.5194/gmd-9-1627-2016, 2016.

Hersbach, H., Bell, B., Berrisford, P., Hirahara, S., Horányi, A., Muñoz-Sabater, J., Nicolas, J., Peubey, C., Radu, R., Schepers, D., et al.:
660 The ERA5 global reanalysis, Quarterly Journal of the Royal Meteorological Society, 146, 1999–2049, 2020.

Hughes, E. J., Sparling, L. C., Carn, S. A., and Krueger, A. J.: Using horizontal transport characteristics to infer an emission height time series of volcanic SO2, Journal of Geophysical Research: Atmospheres, 117, https://doi.org/https://doi.org/10.1029/2012JD017957, 2012.

Huijnen, V., Williams, J., Weele, M. v., Noije, T. v., Krol, M., Dentener, F., Segers, A., Houweling, S., Peters, W., Laat, J. d., et al.: The global chemistry transport model TM5: description and evaluation of the tropospheric chemistry version 3.0, Geoscientific Model Development,
665 3, 445–473, 2010.

Ishii, K., Hayashi, Y., and Shimbori, T.: Using Himawari-8, estimation of SO_2 cloud altitude at Aso volcano eruption, on October 8, 2016, Earth, Planets and Space, 70, 1–9, 2018.

Kilbride, B. M., Edmonds, M., and Biggs, J.: Observing eruptions of gas-rich compressible magmas from space, Nature Communications, 7, 13 744, 2016.

670 Kremser, S., Thomason, L. W., von Hobe, M., Hermann, M., Deshler, T., Timmreck, C., Toohey, M., Stenke, A., Schwarz, J. P., Weigel, R., et al.: Stratospheric aerosol—Observations, processes, and impact on climate, Reviews of Geophysics, 54, 278–335, 2016.

Kristiansen, N., Stohl, A., Prata, A., Richter, A., Eckhardt, S., Seibert, P., Hoffmann, A., Ritter, C., Bitar, L., Duck, T., et al.: Remote sensing and inverse transport modeling of the Kasatochi eruption sulfur dioxide cloud, Journal of Geophysical Research: Atmospheres, 115, 2010.

Lawson, C. L. and Hanson, R. J.: Solving least squares problems, SIAM, 1995.

675 Li, C., Krotkov, N. A., Carn, S., Zhang, Y., Spurr, R. J., and Joiner, J.: New-generation NASA Aura Ozone Monitoring Instrument (OMI) volcanic SO_2 dataset: Algorithm description, initial results, and continuation with the Suomi-NPP Ozone Mapping and Profiler Suite (OMPS), Atmospheric Measurement Techniques, 10, 445–458, 2017.

Li, C., Krotkov, N. A., Leonard, P., and Joiner, J.: OMPS/NPP PCA SO2 Total Column 1-Orbit L2 Swath 50x50km V2, Greenbelt, MD, USA, Goddard Earth Sciences Data and Information Services Center (GES DISC),
680 https://disc.gsfc.nasa.gov/datasets/OMPS_NPP_NMSO2_PCA_L2_2/summary, 2020a.

Li, C., Krotkov, N. A., Leonard, P. J., Carn, S., Joiner, J., Spurr, R. J., and Vasilkov, A.: Version 2 Ozone Monitoring Instrument SO_2 product (OMSO2 V2): new anthropogenic SO_2 vertical column density dataset, Atmospheric Measurement Techniques, 13, 6175–6191, 2020b.

Mailler, S., Menut, L., Khvorostyanov, D., Valari, M., Couvidat, F., Siour, G., Turquety, S., Briant, R., Tuccella, P., Bessagnet, B., et al.: CHIMERE-2017: from urban to hemispheric chemistry-transport modeling, Geoscientific Model Development, 10, 2397–2423, 2017.

685 Marshall, L. R., Maters, E. C., Schmidt, A., Timmreck, C., Robock, A., and Toohey, M.: Volcanic effects on climate: recent advances and future avenues, Bulletin of Volcanology, 84, 54, https://doi.org/10.1007/s00445-022-01559-3, 2022.

Merucci, L., Burton, M., Corradini, S., and Salerno, G. G.: Reconstruction of SO2 flux emission chronology from space-based measurements, Journal of Volcanology and Geothermal Research, 206, 80–87, https://doi.org/https://doi.org/10.1016/j.jvolgeores.2011.07.002, 2011.

Moxnes, E. D., Kristiansen, N. I., Stohl, A., Clarisse, L., Durant, A., Weber, K., and Vogel, A.: Separation of ash and sulfur dioxide during the 2011 Grímsvötn eruption, Journal of Geophysical Research: Atmospheres, 119, 7477–7501, https://doi.org/https://doi.org/10.1002/2013JD021129, 2014.

Mueller, W., Cowie, H., Horwell, C. J., Hurley, F., and Baxter, P. J.: Health Impact Assessment of Volcanic Ash Inhalation: A Comparison With Outdoor Air Pollution Methods, GeoHealth, 4, e2020GH000 256, https://doi.org/https://doi.org/10.1029/2020GH000256, 2020.

Oppenheimer, C.: Ultraviolet sensing of volcanic sulfur emissions, Elements, 6, 87–92, 2010.

Oppenheimer, C., Scaillet, B., and Martin, R. S.: Sulfur degassing from volcanoes: source conditions, surveillance, plume chemistry and earth system impacts, Reviews in Mineralogy and Geochemistry, 73, 363–421, 2011.

Oppenheimer, C., Fischer, T., and Scaillet, B.: 4.4 - Volcanic Degassing: Process and Impact, in: Treatise on Geochemistry (Second Edition), edited by Holland, H. D. and Turekian, K. K., pp. 111–179, Elsevier, Oxford, second edition edn., https://doi.org/https://doi.org/10.1016/B978-0-08-095975-7.00304-1, 2014.

Pardini, F., Burton, M., de' Michieli Vitturi, M., Corradini, S., Salerno, G., Merucci, L., and Di Grazia, G.: Retrieval and intercomparison of volcanic SO2 injection height and eruption time from satellite maps and ground-based observations, Journal of Volcanology and Geothermal Research, 331, 79–91, https://doi.org/https://doi.org/10.1016/j.jvolgeores.2016.12.008, 2017.

Powers, J. G., Klemp, J. B., Skamarock, W. C., Davis, C. A., Dudhia, J., Gill, D. O., Coen, J. L., Gochis, D. J., Ahmadov, R., Peckham, S. E., et al.: The weather research and forecasting model: Overview, system efforts, and future directions, Bulletin of the American Meteorological Society, 98, 1717–1737, 2017.

Prata, A.: Infrared radiative transfer calculations for volcanic ash clouds, Geophysical research letters, 16, 1293–1296, 1989.

Prata, A. and Grant, I.: Retrieval of microphysical and morphological properties of volcanic ash plumes from satellite data: Application to Mt Ruapehu, New Zealand, Quarterly Journal of the Royal Meteorological Society, 127, 2153–2179, 2001.

Prata, A. and Tupper, A.: Aviation hazards from volcanoes: the state of the science, 2009.

Prata, A., Carn, S., Stohl, A., and Kerkmann, J.: Long range transport and fate of a stratospheric volcanic cloud from Soufrière Hills volcano, Montserrat, Atmospheric Chemistry and Physics, 7, 5093–5103, 2007.

Prata, A. J.: Satellite detection of hazardous volcanic clouds and the risk to global air traffic, Natural hazards, 51, 303–324, 2009.

Queißer, M., Burton, M., Theys, N., Pardini, F., Salerno, G., Caltabiano, T., Varnam, M., Esse, B., and Kazahaya, R.: TROPOMI enables high resolution SO$_2$ flux observations from Mt. Etna, Italy, and beyond, Scientific reports, 9, 1–12, 2019.

Robock, A.: Volcanic eruptions and climate, Reviews of Geophysics, 38, 191–219, https://doi.org/https://doi.org/10.1029/1998RG000054, 2000.

Shreve, T., Grandin, R., Boichu, M., Garaebiti, E., Moussallam, Y., Ballu, V., Delgado, F., Leclerc, F., Vallée, M., Henriot, N., et al.: From prodigious volcanic degassing to caldera subsidence and quiescence at Ambrym (Vanuatu): the influence of regional tectonics, Scientific reports, 9, 1–13, 2019.

Shreve, T., Grandin, R., and Boichu, M.: Reservoir depressurization driven by passive gas emissions at Ambrym volcano, Earth and Planetary Science Letters, 584, 117 512, 2022.

Simpson, J. J., Hufford, G., Pieri, D., and Berg, J.: Failures in Detecting Volcanic Ash from a Satellite-Based Technique, Remote Sensing of Environment, 72, 191–217, https://doi.org/https://doi.org/10.1016/S0034-4257(99)00103-0, 2000.

Sparks, R.: Dynamics of magma degassing, Geological Society, London, Special Publications, 213, 5–22, 2003.

725 Stein, A., Draxler, R. R., Rolph, G. D., Stunder, B. J., Cohen, M., and Ngan, F.: NOAA's HYSPLIT atmospheric transport and dispersion modeling system, Bulletin of the American Meteorological Society, 96, 2059–2077, 2015.

Stewart, C., Damby, D. E., Horwell, C. J., Elias, T., Ilyinskaya, E., Tomašek, I., Longo, B. M., Schmidt, A., Carlsen, H. K., Mason, E., Baxter, P. J., Cronin, S., and Witham, C.: Volcanic air pollution and human health: recent advances and future directions, Bulletin of Volcanology, 84, 11, https://doi.org/10.1007/s00445-021-01513-9, 2021.

730 Stoffelen, A., Pailleux, J., Källén, E., Vaughan, J. M., Isaksen, L., Flamant, P., Wergen, W., Andersson, E., Schyberg, H., Culoma, A., et al.: The atmospheric dynamics mission for global wind field measurement, Bulletin of the American Meteorological Society, 86, 73–88, 2005.

Stohl, A., Prata, A., Eckhardt, S., Clarisse, L., Durant, A., Henne, S., Kristiansen, N. I., Minikin, A., Schumann, U., Seibert, P., et al.: Determination of time-and height-resolved volcanic ash emissions and their use for quantitative ash dispersion modeling: the 2010 Eyjafjallajökull eruption, Atmospheric Chemistry and Physics, 11, 4333–4351, 2011.

735 Surono, Jousset, P., Pallister, J., Boichu, M., Buongiorno, M. F., Budisantoso, A., Costa, F., Andreastuti, S., Prata, F., Schneider, D., Clarisse, L., Humaida, H., Sumarti, S., Bignami, C., Griswold, J., Carn, S., Oppenheimer, C., and Lavigne, F.: The 2010 explosive eruption of Java's Merapi volcano—A '100-year' event, Journal of Volcanology and Geothermal Research, 241-242, 121–135, 2012.

Theys, N., Campion, R., Clarisse, L., Brenot, H., Gent, J. v., Dils, B., Corradini, S., Merucci, L., Coheur, P.-F., Roozendael, M. V., et al.: Volcanic SO$_2$ fluxes derived from satellite data: a survey using OMI, GOME-2, IASI and MODIS, Atmospheric Chemistry and Physics,
740 13, 5945–5968, 2013.

Theys, N., De Smedt, I., Van Gent, J., Danckaert, T., Wang, T., Hendrick, F., Stavrakou, T., Bauduin, S., Clarisse, L., Li, C., et al.: Sulfur dioxide vertical column DOAS retrievals from the Ozone Monitoring Instrument: Global observations and comparison to ground-based and satellite data, Journal of Geophysical Research: Atmospheres, 120, 2470–2491, 2015.

Theys, N., Smedt, I. D., Yu, H., Danckaert, T., Gent, J. v., Hörmann, C., Wagner, T., Hedelt, P., Bauer, H., Romahn, F., et al.: Sulfur dioxide
745 retrievals from TROPOMI onboard Sentinel-5 Precursor: algorithm theoretical basis, Atmospheric Measurement Techniques, 10, 119–153, 2017.

Theys, N., Hedelt, P., De Smedt, I., Lerot, C., Yu, H., Vlietinck, J., Pedergnana, M., Arellano, S., Galle, B., Fernandez, D., et al.: Global monitoring of volcanic SO$_2$ degassing with unprecedented resolution from TROPOMI onboard Sentinel-5 Precursor, Scientific reports, 9, 1–10, 2019.

750 Theys, N., Fioletov, V., Li, C., De Smedt, I., Lerot, C., McLinden, C., Krotkov, N., Griffin, D., Clarisse, L., Hedelt, P., Loyola, D., Wagner, T., Kumar, V., Innes, A., Ribas, R., Hendrick, F., Vlietinck, J., Brenot, H., and Van Roozendael, M.: A sulfur dioxide Covariance-Based Retrieval Algorithm (COBRA): application to TROPOMI reveals new emission sources, Atmospheric Chemistry and Physics, 21, 16 727–16 744, https://doi.org/10.5194/acp-21-16727-2021, 2021.

Thomas, H. E. and Watson, I.: Observations of volcanic emissions from space: current and future perspectives, Natural Hazards, 54, 323–354,
755 2010.

Thorsteinsson, T., Jóhannsson, T., Stohl, A., and Kristiansen, N. I.: High levels of particulate matter in Iceland due to direct ash emissions by the Eyjafjallajökull eruption and resuspension of deposited ash, Journal of Geophysical Research: Solid Earth, 117, https://doi.org/https://doi.org/10.1029/2011JB008756, 2012.

Veefkind, J., Aben, I., McMullan, K., Förster, H., De Vries, J., Otter, G., Claas, J., Eskes, H., De Haan, J., Kleipool, Q., et al.: TROPOMI
760 on the ESA Sentinel-5 Precursor: A GMES mission for global observations of the atmospheric composition for climate, air quality and ozone layer applications, Remote sensing of environment, 120, 70–83, 2012.

Vira, J., Carboni, E., Grainger, R. G., and Sofiev, M.: Variational assimilation of IASI SO$_2$ plume height and total column retrievals in the 2010 eruption of Eyjafjallajökull using the SILAM v5.3 chemistry transport model, Geoscientific Model Development, 10, 1985–2008, https://doi.org/10.5194/gmd-10-1985-2017, 2017.

765 Weinzierl, B., Sauer, D., Minikin, A., Reitebuch, O., Dahlkötter, F., Mayer, B., Emde, C., Tegen, I., Gasteiger, J., Petzold, A., Veira, A., Kueppers, U., and Schumann, U.: On the visibility of airborne volcanic ash and mineral dust from the pilot's perspective in flight, Physics and Chemistry of the Earth, Parts A/B/C, 45-46, 87–102, https://doi.org/https://doi.org/10.1016/j.pce.2012.04.003, 2012.

Yang, K., Krotkov, N. A., Krueger, A. J., Carn, S. A., Bhartia, P. K., and Levelt, P. F.: Retrieval of large volcanic SO$_2$ columns from the Aura Ozone Monitoring Instrument: Comparison and limitations, Journal of Geophysical Research: Atmospheres, 112, 2007.

770 Yang, K., Liu, X., Bhartia, P. K., Krotkov, N. A., Carn, S. A., Hughes, E. J., Krueger, A. J., Spurr, R. J. D., and Trahan, S. G.: Direct retrieval of sulfur dioxide amount and altitude from spaceborne hyperspectral UV measurements: Theory and application, Journal of Geophysical Research: Atmospheres, 115, https://doi.org/https://doi.org/10.1029/2010JD013982, 2010.

Yang, K., Dickerson, R. R., Carn, S. A., Ge, C., and Wang, J.: First observations of SO$_2$ from the satellite Suomi NPP OMPS: Widespread air pollution events over China, Geophysical Research Letters, 40, 4957–4962, 2013.

775 Zhang, Y., Li, C., Krotkov, N. A., Joiner, J., Fioletov, V., and McLinden, C.: Continuation of long-term global SO2 pollution monitoring from OMI to OMPS, Atmospheric Measurement Techniques, 10, 1495–1509, https://doi.org/10.5194/amt-10-1495-2017, 2017.

Zidikheri, M. J. and Potts, R. J.: A simple inversion method for determining optimal dispersion model parameters from satellite detections of volcanic sulfur dioxide, Journal of Geophysical Research: Atmospheres, 120, 9702–9717, https://doi.org/https://doi.org/10.1002/2015JD023627, 2015.
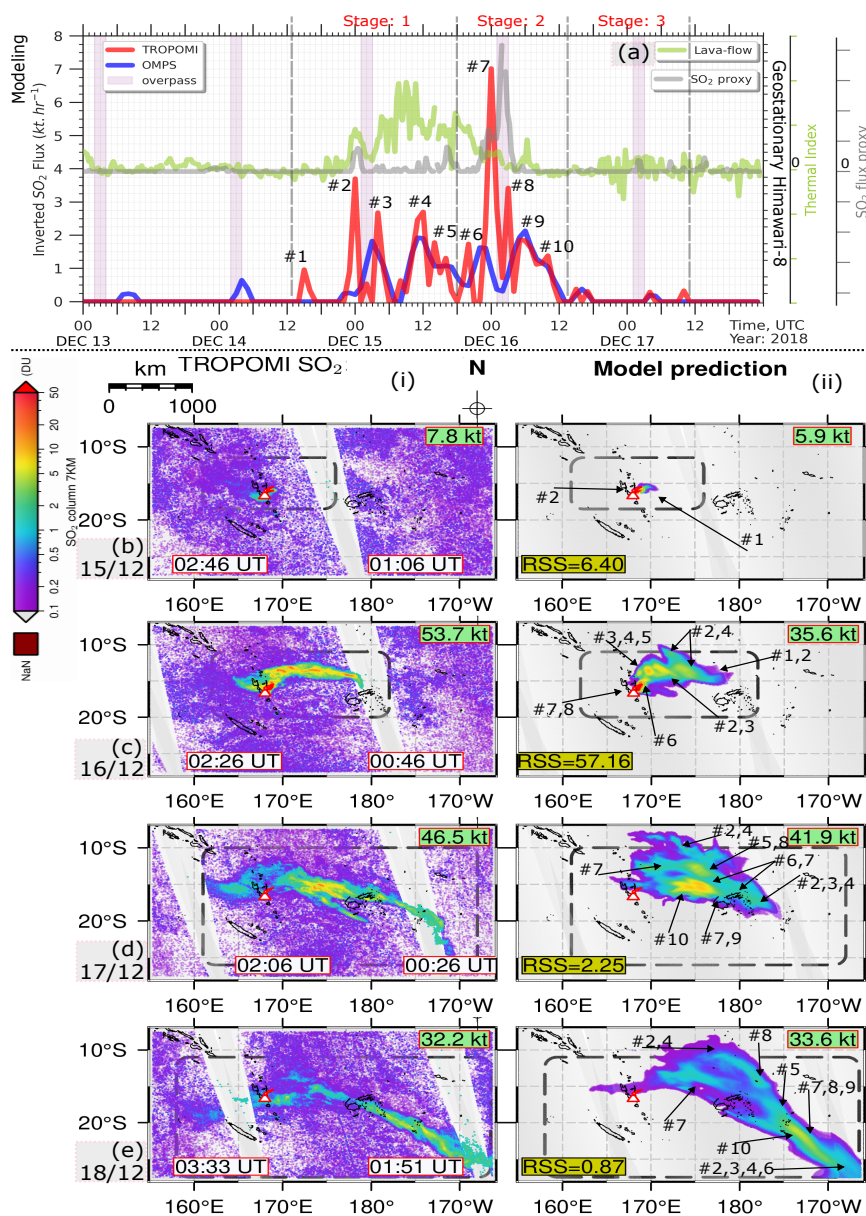
Figure 1. Inverse modeling results: (a) Hourly-resolved SO$_2$ mass-flux ($\mathrm{kt\,h^{-1}}$) from Ambrym by assimilating six consecutive images from TROPOMI and OMPS, respectively, taken between December 13–18, 2018. The two satellites' simultaneous overpass time is indicated with a light pink shade. The TROPOMI-derived time series (red line) produces strong pulses of SO$_2$ emissions, numbered #T1 through #T10. Time series of the thermal index associated with lava flow pixels (green line) and qualitative SO$_2$ flux proxy (gray line), both derived from Himawari-8/AHI are also shown. The SO$_2$ columns for December 15–18 (b–e) are illustrated from TROPOMI (i), together with the associated model simulations, i.e., initializing the CTM simulation with the SO$_2$ sources acquired through inverse modeling (ii). The inverted SO$_2$ injection heights are detailed in Fig. 3. The arrows link the emissions noted in the SO$_2$ mass-flux time series (a) to the corresponding SO$_2$ parcels (b–e). The analysis residual squared sum (RSS) between observation and CTM simulation, satellite orbit time tags in UT, and SO$_2$ mass (kt) within the dashed box are provided. SO$_2$ maps for 13–14 December can be found in Fig. S7.
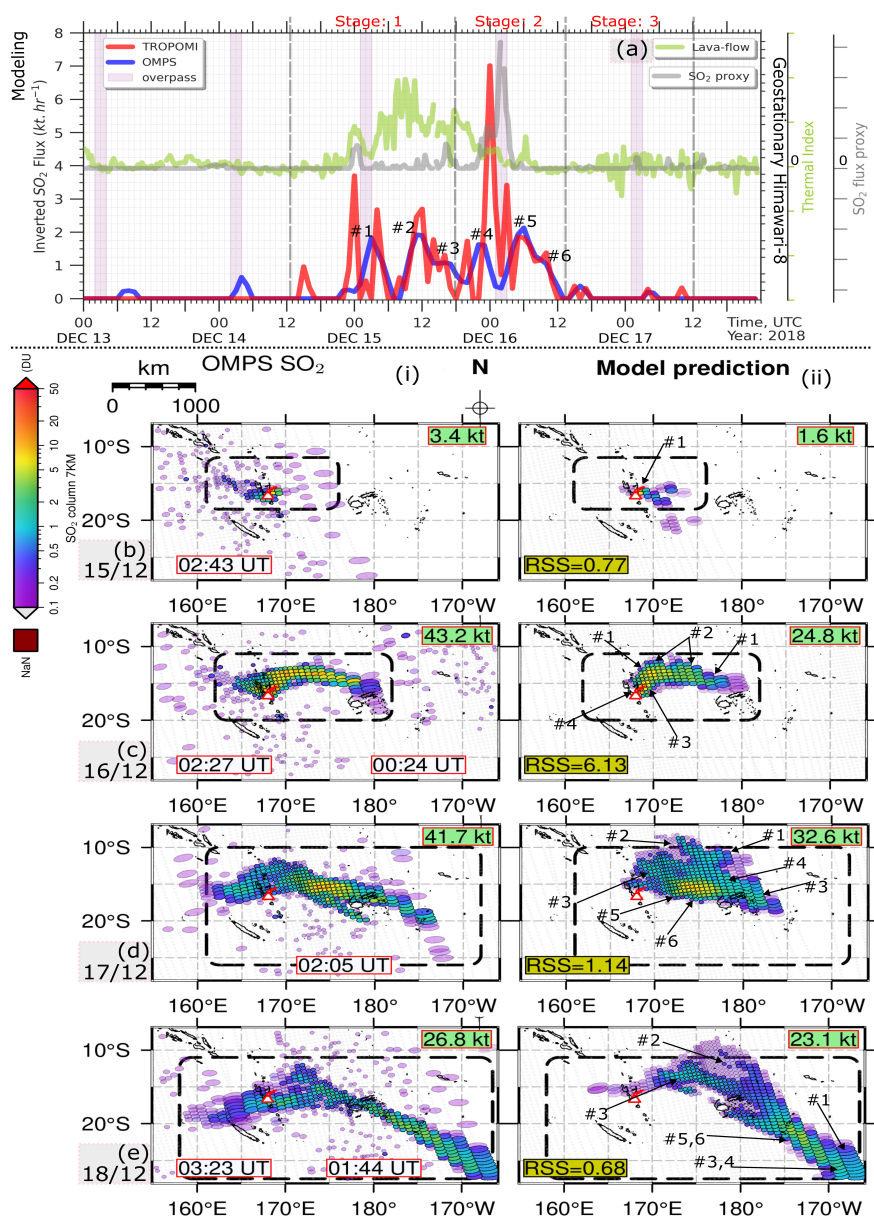
Figure 2. Similar to Fig. 1, but for the inverse modeling of OMPS SO2 columns (blue line). OMPS has a coarser spatial resolution than TROPOMI, which can cause footprint distortions when the scan lines are near the edge of the swath.
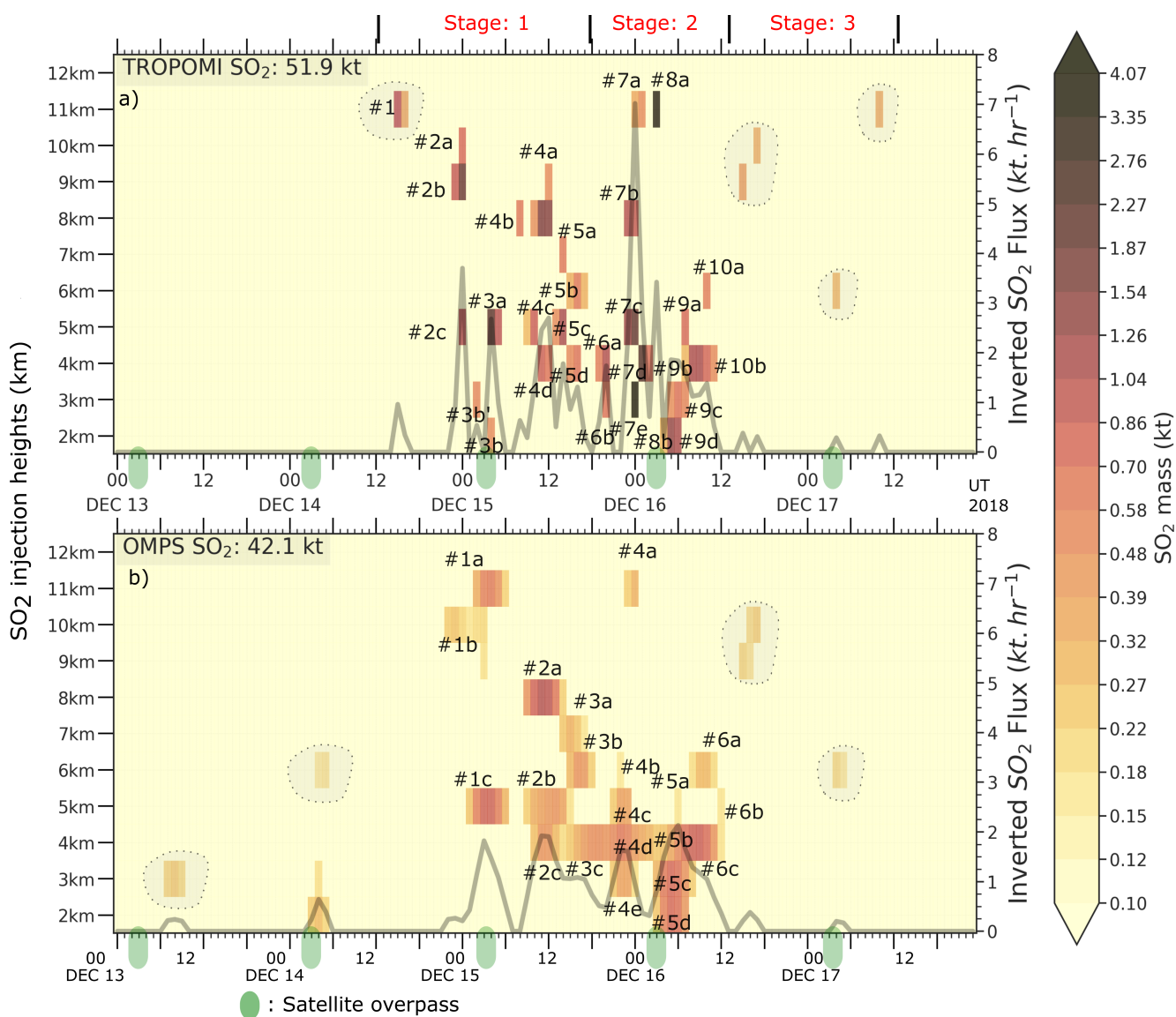
Figure 3. SO₂ emission rates by inverse modeling (identical to Figs. 1a, 2a) for the 2018 Ambrym eruption at hourly temporal resolution, showing SO₂ mass (kt) and corresponding injection heights (km). Numbered emissions (#) are labeled in alphabetical order to indicate multiple SO₂ injection heights. Ambiguous SO₂ injection heights are contoured in gray. Satellite overpass times are also indicated.
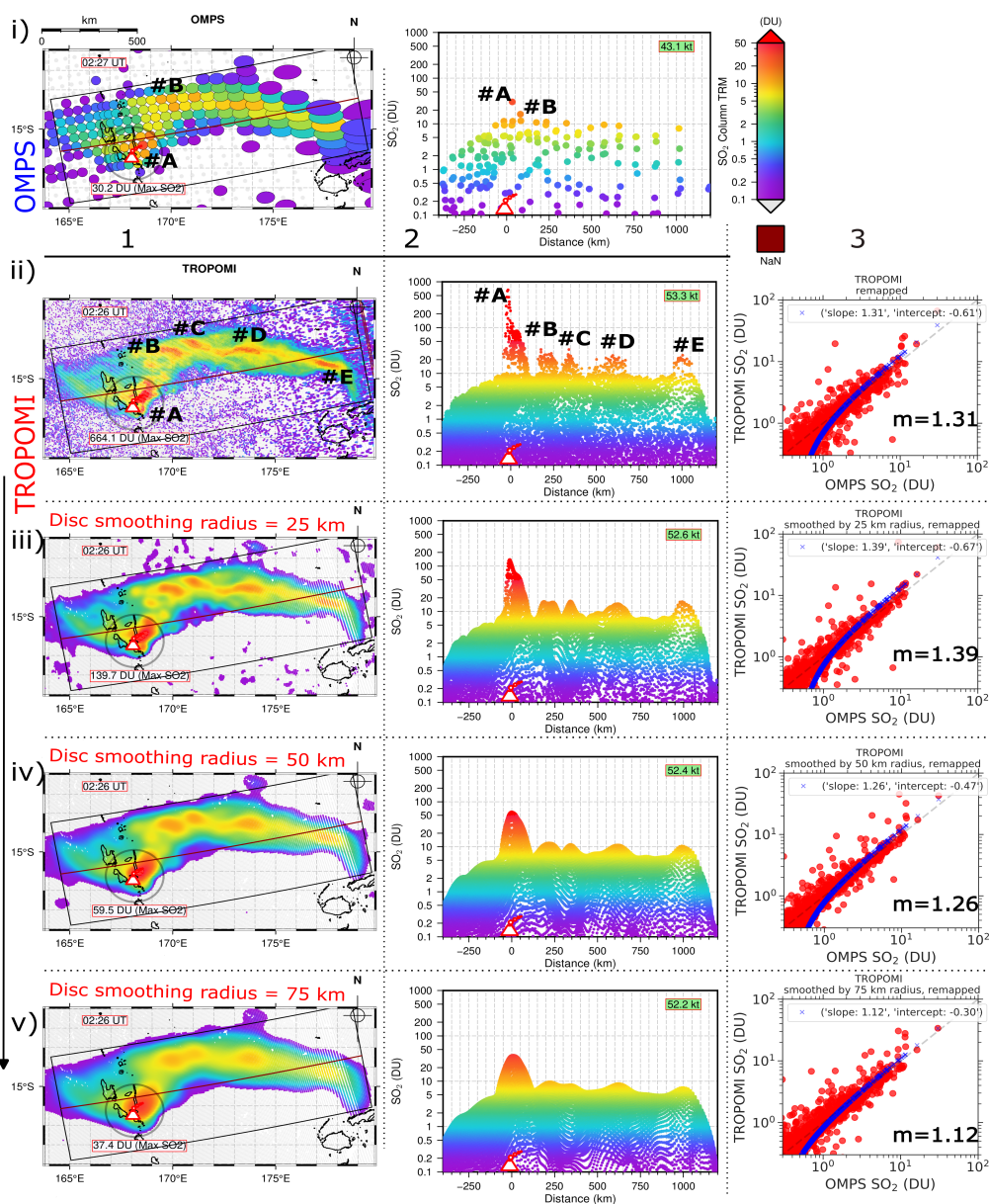
Figure 4. Ambrym dispersed SO$_2$-rich plume on December 16, 2018, at about 02:30UT, observed from OMPS (i) and TROPOMI (ii). The maximum SO$_2$ column within a radius of $150\,\text{km}$ around the source is indicated in a rectangular box with a red border. TROPOMI data are smoothed over disks with radii of (iii) 25, (iv) 50, and (v) $75\,\text{km}$, respectively. The first column (1) shows the maps of the SO$_2$ column. Color-shaded ellipses represent the satellite-measured SO$_2$ column and the corresponding footprint. The gray dots indicate the center of the footprint for the SO$_2$ column less than $0.1\,\text{DU}$. The footprint gradually stretches horizontally with increasing longitude because of the large viewing zenith angle and the curvature of the Earth. The second column (2) depicts the eastward plume transect. This transect encompasses pixels within a rectangular box ($1200\,\text{km} \times 600\,\text{km}$). These pixels are projected onto the central axis, positioned in the middle of the box. In the top right corner of each panel, we show the SO$_2$ mass (kt) contained within this rectangular box. The third column (3) refers to the linear regression between TROPOMI observations, after smoothing and remapping onto the OMPS grid, and OMPS raw SO$_2$ column data. The linear regression data is based on the measurements on December 13–18, 2018. The slope of the linear fit is denoted by "m".
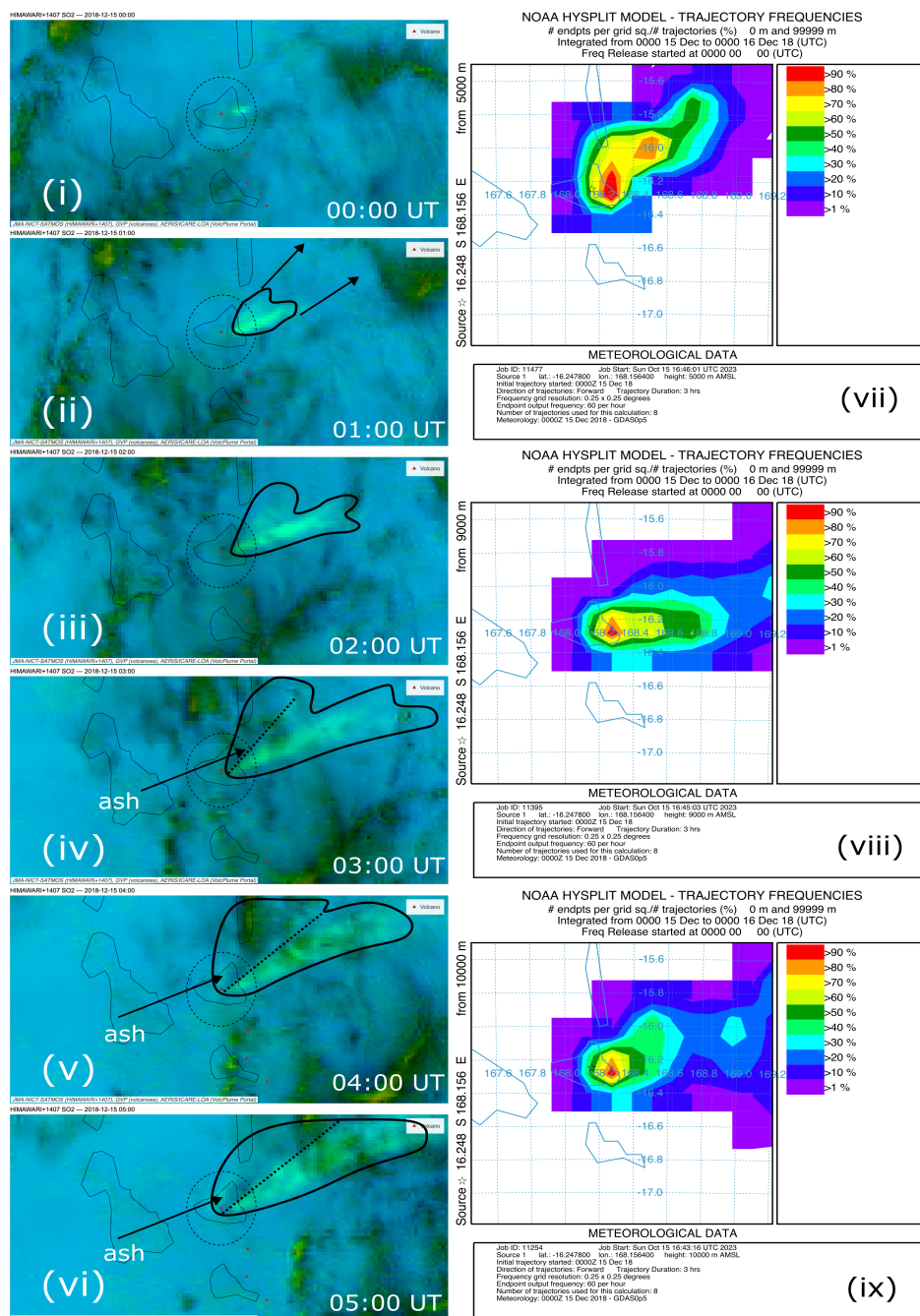
Figure 5. Himawari-8/AHI SO₂ RGB compositions for the Ambrym plume on December 15 show the hourly evolution of the two branches of the SO₂ plume from 00:00 UT until 05:00 UT (left panel, i-vi). The black contour line shows the two strong wind shears at different altitudes that caused the ash and SO₂ to separate, as indicated in iv–vi. The right panel shows the HYSPLIT trajectory frequencies when initialized at 5 km (vii), 9 km (viii), and 10 km (ix) ASL at 00:00 UT on December 15, using 0.5-degree GDAS reanalysis data.
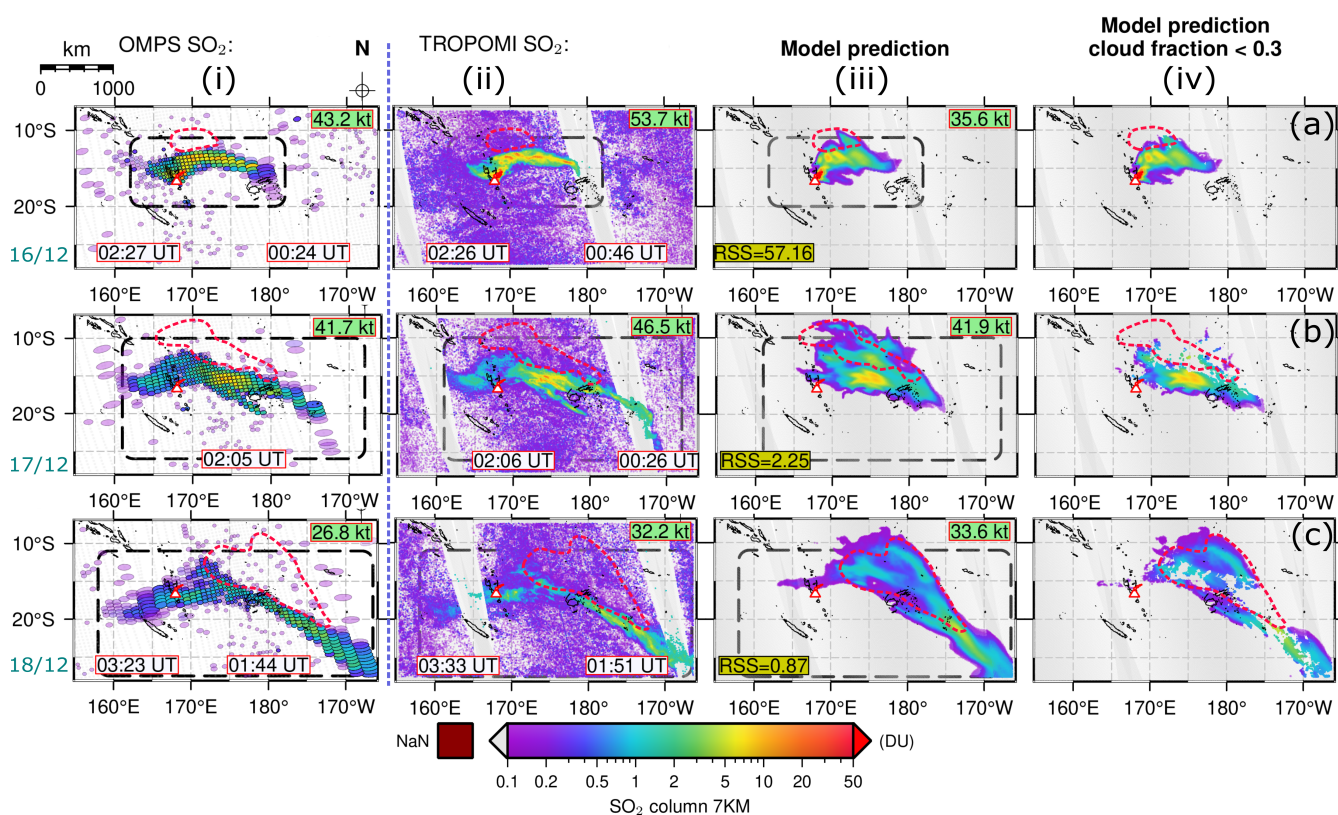
Figure 6. Illustration of the cloud cover over the north and northeast sections of Ambrym's volcanic SO₂ plume on December 16 (a), 17 (b), and 18 (c), outlined in red. It features SO₂ column measurements from OMPS (i) and TROPOMI (ii), the CHIMERE CTM simulation initialized with TROPOMI-derived SO₂ flux emissions (iii), and the same simulation after implementing a cloud fraction cutoff of 0.3 (iv).
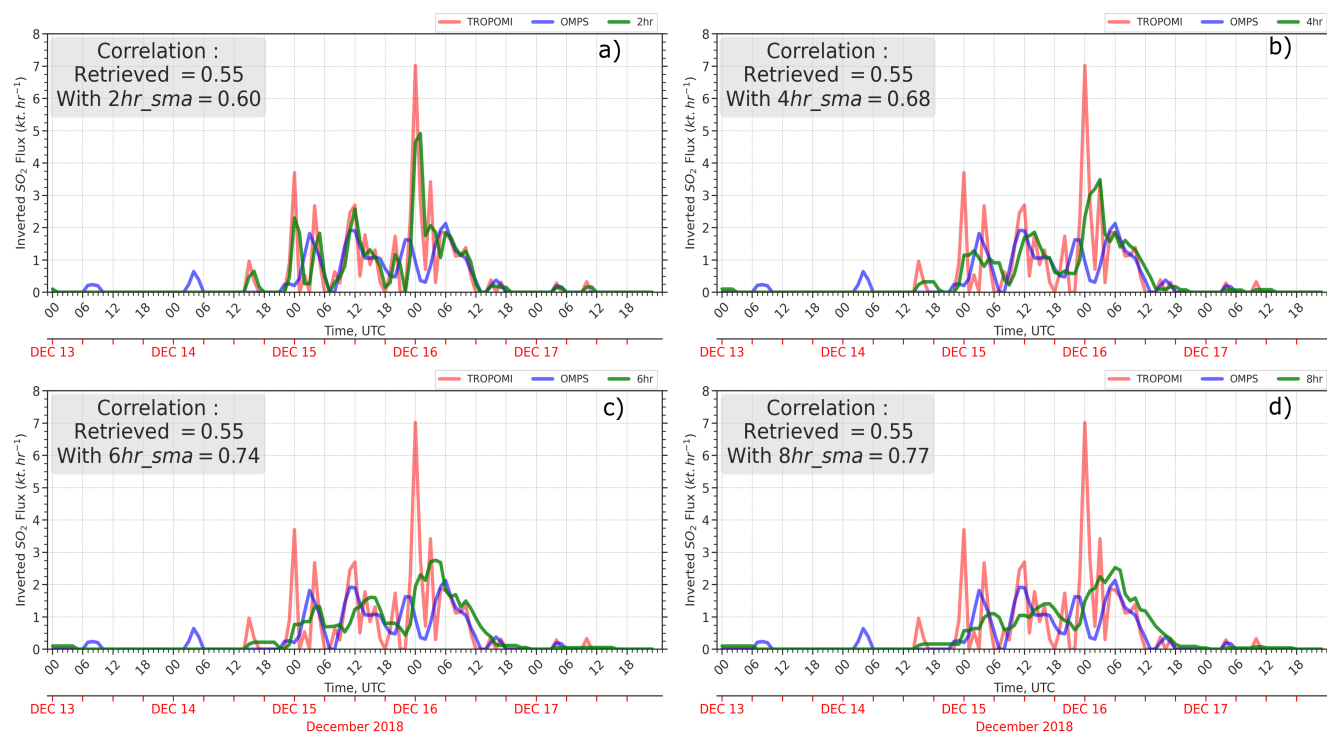
Figure 7. Pearson product-moment correlation coefficients between OMPS-derived SO$_2$ flux time series and TROPOMI-derived SO$_2$ flux time series are presented. The TROPOMI-derived SO$_2$ flux time series is subject to smoothing using a simple moving average (SMA) time window of (a) 2 hours, (b) 4 hours, (c) 6 hours, and (d) 8 hours. The text boxes within each panel show the correlation values both before (retrieved) and after applying the SMA to the TROPOMI-derived SO$_2$ flux time series.